



Published in final edited form as:

ACS Appl Bio Mater. 2019 July 15; 2(7): 2964–2977. doi:10.1021/acsabm.9b00312.

## A New Class of Homoleptic and Heteroleptic Bis(terpyridine) Iridium(III) Complexes with Strong Photodynamic Therapy Effects

Bingqing Liu<sup>†</sup>, Susan Monro<sup>‡</sup>, Zhike Li<sup>¥</sup>, Mohammed A. Javed<sup>†</sup>, Daniel Ramirez<sup>†</sup>, Colin G. Cameron<sup>§</sup>, Katsuya Colón<sup>§</sup>, John Roque III<sup>§</sup>, Svetlana Kilina<sup>†</sup>, Jian Tian<sup>\*,¥</sup>, Sherri A. McFarland<sup>\*,‡,§</sup>, Wenfang Sun<sup>\*,†</sup>

<sup>†</sup>Department of Chemistry and Biochemistry, North Dakota State University, Fargo, ND 58108–6050, USA.

<sup>‡</sup>Department of Chemistry, Acadia University, 6 University Avenue, Wolfville, NS B4P 2R6, Canada.

<sup>¥</sup>Key Laboratory of Combinatorial Biosynthesis and Drug Discovery (MOE), Hubei Province Engineering and Technology Research Center for Fluorinated Pharmaceuticals, School of Pharmaceutical Sciences, Wuhan University, Wuhan 430071, P. R. China

<sup>§</sup>Department of Chemistry and Biochemistry, University of North Carolina at Greensboro, Greensboro, NC 27402–6170, USA.

### Abstract

Six homo- or heteroleptic tricationic Ir(R<sub>1</sub>-tpy)(R<sub>2</sub>-tpy)<sup>3+</sup> complexes (**Ir1–Ir6**, R<sub>1</sub>/R<sub>2</sub> = Ph, 4'-N(CH<sub>3</sub>)<sub>2</sub>Ph, pyren-1-yl, or 4'-{2-[2-(2-methoxyethoxy)ethoxy]ethoxy}Ph, tpy = 2,2';6',2''-terpyridine) were synthesized and tested for photodynamic therapy (PDT) effects. The ground- and excited-state characteristics of these complexes were studied systematically *via* spectroscopic methods and quantum chemistry calculations. All complexes possessed intraligand charge transfer (<sup>1</sup>ILCT) / metal-to-ligand charge transfer (<sup>1</sup>MLCT) dominated transition(s) in their low-energy absorption bands, which red-shifted with the increased electron-releasing strength of the R<sub>1</sub>/R<sub>2</sub> substituent. Five of the complexes exhibited ligand-centered <sup>3</sup>π,π\*<sup>β</sup>ILCT/<sup>3</sup>MLCT emission. With a stronger electron-releasing R<sub>1</sub>/R<sub>2</sub> substituent, the degree of charge transfer contribution increased, leading to a decrease of the emission quantum yield. When the 4'-N(CH<sub>3</sub>)<sub>2</sub>Ph substituent was introduced on both tpy ligands, the emission of **Ir3** was completely quenched. Our

\*Corresponding Author Wenfang.Sun@ndsu.edu. Telephone: 701-231-6254. Fax: 701-231-8831., samcfarland@uncg.edu. Telephone: 336-256-1080. Fax: 336-334-5402., jian.tian@whu.edu.cn.

#### ASSOCIATED CONTENT

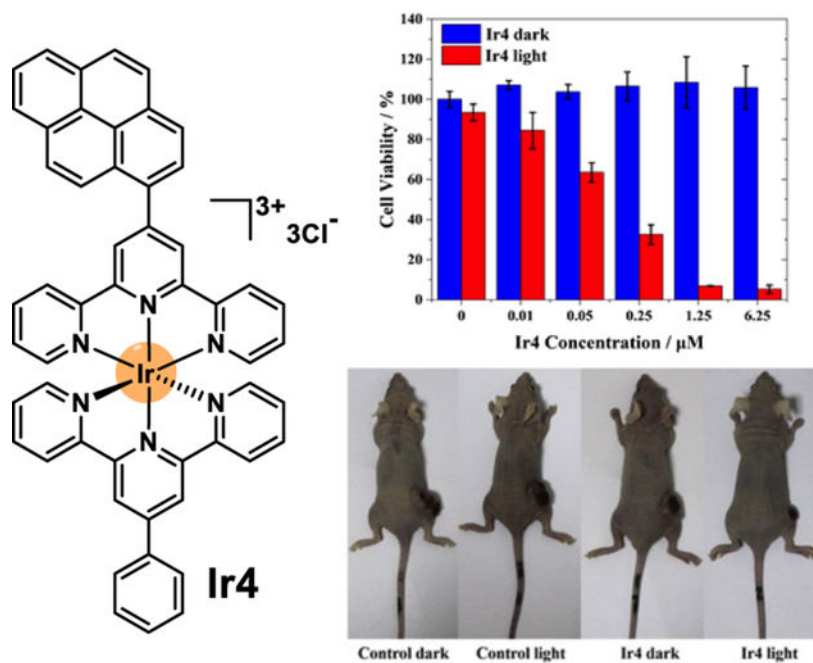
**Supporting Information.** Experimental details for the PDT studies on SK-MEL-28 cells and on MCF-7 breast cancer cells and its xenograft tumor model; comparison of the UV-vis absorption spectra obtained experimentally and by calculation for complexes **Ir1–Ir6** in CH<sub>3</sub>CN; the normalized UV-vis absorption and emission spectra of **Ir1–Ir6** in different solvents; the comparison of the emission spectra of **Ir4** in aerated and deaerated acetonitrile solutions; the natural transition orbitals (NTOs) for the major transitions contributing to the absorption bands of **Ir1–Ir6** at 280–360 nm in CH<sub>3</sub>CN; the emission characteristics of **Ir1–Ir6** in different solvents; and the time-resolved ns transient absorption spectra of **Ir1–Ir6** in CH<sub>3</sub>CN. This material is available free of charge via the Internet at <http://pubs.acs.org>.

#### Notes

The authors declare no competing financial interest.

study on the transient absorption of these complexes demonstrated that they all possessed broadband triplet excited-state absorption in the 400–800 nm region. Pyrenyl substitution of one or more tpy ligands, as in **Ir4** and **Ir5**, increased the lifetimes of the lowest triplet excited state and the singlet oxygen ( $^1\text{O}_2$ ) production efficiencies. **Ir1–Ir5** were nontoxic toward SK-MEL-28 cells, with photocytotoxicities that varied from 0.18 to 153  $\mu\text{M}$ . Among them, **Ir4** had the highest  $^1\text{O}_2$  quantum yield (0.81) in cell-free conditions, showing the largest photocytotoxicity against SK-MEL-28 cells for Ir(III) PSs to date, and was the most efficient generator of reactive oxygen species (ROS) *in vitro*. **Ir4** possessed a very large phototherapeutic index (PI = dark  $\text{EC}_{50}$  / light  $\text{EC}_{50}$ ) of >1657, the largest reported for an Ir(III) complex photosensitizer upon broadband visible light (400–700 nm) activation. **Ir4** also exhibited a very strong PDT effect toward MCF-7 breast cancer cells and its xenograft tumor model. Upon 450-nm light activation, **Ir4** dramatically inhibited the xenograft tumor growth and exhibited negligible side effects upon PDT treatment.

## Graphical Abstract



## Keywords

Bis(terpyridine) iridium(III) complex; Photophysics; Photodynamic therapy; Photobiological activity; Reactive oxygen species; Absorption; Emission; Transient absorption

## INTRODUCTION

Photodynamic therapy (PDT), a noninvasive and spatiotemporally selective anticancer strategy, has attracted continued interest over the past a few decades.<sup>1,2</sup> PDT depends on the interaction of a photosensitizer (PS) and oxygen upon light activation to generate cytotoxic singlet oxygen ( $^1\text{O}_2$ ) via energy transfer (type II) or other reactive oxygen species (ROS) via electron transfer (type I), from the excited triplet state of a photosensitizer (PS).<sup>3</sup> The

sensitized  $^1\text{O}_2$  and/or other ROS species irreversibly damage(s) tumor cells, tumor vasculature, and have/has the capacity to invoke an antitumor immune response. Because the PS plays a critical role in PDT, the search for better PSs with effective  $^1\text{O}_2$  and/or ROS generation is an active area of investigation.<sup>4,5</sup>

Porphyrin-based compounds have been widely studied PSs for PDT,<sup>6–9</sup> but the only FDA-approved clinical PS for cancer therapy is Photofrin. Despite its prolific use in the field of PDT, there has been ongoing interest in the development of new PSs with better, or simply different, properties.<sup>10–15</sup> Transition metal complexes in particular have emerged as promising candidates.<sup>5,16–19</sup> In comparison to the porphyrins PSs and other organic PSs, transition metal complex PSs possess some unique merits, such as (i) the ability to tune the singlet and triplet excited state properties independently,<sup>2,5,20</sup> (ii) very high triplet excited state quantum yields, (iii) the opportunity to select coordinating ligands for better thermal and kinetic stability, and (iv) the existence of a number of excited state configurations that can be accessed with visible light.<sup>18</sup> Additionally, many transition metal complexes, such as the Ru(II) and Ir(III) complexes in particular, exhibit bright red to near-infrared phosphorescence for *in situ* monitoring of PS distribution in tumors and cells, providing novel theranostic platforms for imaging-guided PDT and aiding in the mechanistic study of PDT in order to optimize the treatment efficacy.<sup>11,21–27</sup>

Among the variety of transition metal complexes, cationic Ir(III) complexes, with octahedral  $d^6$  geometry, appear promising as theranostic PDT agents due to their high quantum yields for triplet excited state formation and long triplet excited state lifetimes. Together, these facilitate efficient  $^1\text{O}_2$  generation through type II energy transfer with bright intracellular luminescence for imaging.<sup>11,19–27</sup> While Ir(III) is able to form complexes with coordinating or cyclometalating bidentate or terdentate ligands,<sup>11,19–38</sup> only the tris-bidentate Ir(III) complexes featuring various diimine, cyclometalating, or dianionic ligands have been widely studied for theranostic PDT applications.<sup>11,19–36</sup> Investigations of bis-terdentate Ir(III) complexes for PDT are relatively scarce.<sup>39</sup>

The bis(terpyridine) (tpy) coordinated Ir(III) complexes are less studied, in part, due to the harsh reaction conditions required for synthesizing them. However, this arrangement has the advantage of higher geometric symmetry, precluding the formation of stereoisomers. The higher 3+ charge of Ir (versus  $\text{Ru}^{2+}$ ) may improve the solubility of these complexes in water. Among the reported mono- or multi-nuclear Ir(ph-tpy)<sub>2</sub><sup>3+</sup>-based complexes,<sup>40–44</sup> some were demonstrated to exhibit aqueous solubility<sup>41</sup> and have long-lived triplet excited states,<sup>40</sup> which are desirable features for PSs. However, the exploration of these Ir(III) bis(terpyridine) complexes for biological applications is undeveloped.<sup>39,43,45,46</sup>

To the best of our knowledge, the only report on bisterdentate Ir(III) complexes for PDT is a series of dinuclear Ir(III) complexes with fluorenyl-linked ditopic terpyridine as the bridging ligand and various terdentate ligand as the end-capped ligands, which was reported by us.<sup>39</sup> We demonstrated that these complexes could be used as *in vitro* PDT agents toward human SK-MEL-28 melanoma cells when activated with visible light. They possessed submicromolar photocytotoxicity and the phototherapeutic indices (PIs) were of 20 – 288. All of the complexes were brightly phosphoresced when entered compromised cells and

light irradiation enhanced the cellular uptake. These features highlighted the theranostic potential of this new class of Ir(III) complex PSs. We also found that variation of the terminal terdentate ligands drastically altered the photophysical properties and consequently the *in vitro* PDT effects.

Inspired by the aforementioned results, herein we further explore Ir(III) bis(terpyridine) complexes for PDT applications with a focus on the mononuclear Ir(R-tpy)<sub>2</sub><sup>3+</sup> scaffold with different substituents on the tpy ligands. Six hetero- or homoleptic Ir(R<sub>1</sub>-tpy)(R<sub>2</sub>-tpy)<sup>3+</sup> complexes (**Ir1–Ir6** in Chart 1) were synthesized and fully characterized and investigated for their potential as PDT agents. Different 4'-substituted phenyl or pyren-1-yl groups were introduced to the tpy ligand(s) in order to tune the photophysical properties and photobiological activities of this class of Ir(III) PSs. Dimethylaminophenyl and pyren-1-yl substituents were introduced to the tpy ligand(s) to probe the effect of an increase in the intraligand charge transfer (ILCT) character of the excited state, while the 2-[2-(2-methoxyethoxy)ethoxy]ethoxy substituent was appended to one of the phenyl groups to enhance water solubility, which can be visualized by naked eyes.

## EXPERIMENTAL SECTION

### Synthesis and Characterization.

All reagents used in this work were purchased from Sigma–Aldrich or Alfa Aesar and used as received without any further purification. The Al<sub>2</sub>O<sub>3</sub> (activated, neutral) and silica (60 Å, 230–400 mesh) gels used for column chromatography were obtained from Sorbent Technology. The 4-substituted tpy ligands, *i.e.* 4-phenyl-tpy, 4-(4'-dimethylaminophenyl)-tpy, and 4-(pyren-1-yl)-tpy were synthesized from 2-acetylpyridine and corresponding 4-substituted benzaldehyde according to the published procedures.<sup>47–49</sup> Compound 4-{2-[2-(2-methoxyethoxy)ethoxy]ethoxy}benzaldehyde was synthesized from 2-[2-(2-methoxyethoxy)ethoxy]ethanol and 4-methylbenzenesulfonyl chloride following the reported method.<sup>50</sup> Complex 4-ph-tpy–IrCl<sub>3</sub> was prepared based on the literature procedure.<sup>51</sup> The synthesized complexes **Ir1–Ir6** were characterized by <sup>1</sup>H NMR, high-resolution electrospray ionization mass spectrometry (ESI–MS), and elemental analysis. <sup>1</sup>H NMR spectra were recorded on Bruker–400 or Varian Oxford–VNMR (500 MHz) spectrometers. ESI–MS analyses were conducted on a Bruker BioTOF III mass spectrometer. Elemental analyses were carried out by NuMega Resonance Laboratories, Inc. in San Diego, California.

### 4-{4'-[2-[2-(2-methoxyethoxy)ethoxy]ethoxy]phenyl}tpy.

2-Acetylpyridine (2.42 g, 10 mmol), 4-{2-[2-(2-methoxyethoxy)ethoxy]ethoxy}benzaldehyde (2.68 g, 20 mmol), and KOH (1.12 g, 20 mmol) were added to EtOH solution. Then the mixture reacted at room temperature for 2 hours under stirring. After that, ammonium hydroxide (20 ml, 28% NH<sub>3</sub> aqueous solution) was added into the mixture, and the solution was brought to reflux for 24 hours. After cooling to room temperature, the solution was poured to water, then the crude product was extracted by dichloromethane. After drying the dichloromethane layer and removing the solvent, the crude product was separated on a silica gel column eluted with ethyl acetate/

hexane (1:1, v/v) to obtain a yellow oil as the target compound (1.51 g, 32%).  $^1\text{H NMR}$  (500 MHz,  $\text{CDCl}_3$ ):  $\delta$  8.76–8.72 (m, 2H), 8.71 (s, 2H), 8.67 (dd,  $J = 7.9, 0.8$  Hz, 2H), 7.87 (d,  $J = 8.7$  Hz, 4H), 7.38–7.32 (m, 2H), 7.05 (d,  $J = 8.5$  Hz, 2H), 4.24–4.18 (m, 2H), 3.94–3.89 (m, 2H), 3.77 (dd,  $J = 5.7, 3.9$  Hz, 2H), 3.71 (dd,  $J = 5.5, 3.8$  Hz, 2H), 3.69–3.65 (m, 2H), 3.57 (dd,  $J = 5.5, 3.7$  Hz, 2H), 3.39 (s, 3H).

### General Synthetic Procedure for 4-(4'-R-phenyl)tpy-IrCl<sub>3</sub>.

A degassed ethylene glycol suspension of the corresponding 4-(4'-R-phenyl)tpy (0.1 mmol, R = dimethylamino or pyren-1-yl) and  $\text{IrCl}_3 \cdot \text{H}_2\text{O}$  (0.1 mmol) was heated to 160 °C in dark. After 15 minutes, the mixture was cooled to room temperature. The formed precipitate was filtered out and washed with water (10 mL  $\times$  2) and ethanol (10 mL  $\times$  2), and dried in vacuum. The obtained solid was then used for the next step reaction without further purification.

**4-(4'-Dimethylaminophenyl)tpy-IrCl<sub>3</sub>.**—A dark red powder was obtained as the product (41 mg, 63%).  $^1\text{H NMR}$  (400 MHz, DMSO):  $\delta$  9.21 (dd,  $J = 5.6, 1.0$  Hz, 2H), 8.97 (s, 2H), 8.89 (d,  $J = 8.1$  Hz, 2H), 8.27 (td,  $J = 7.9, 1.5$  Hz, 2H), 8.13 (d,  $J = 9.0$  Hz, 2H), 7.97–7.89 (m, 2H), 6.93 (d,  $J = 9.1$  Hz, 2H), 3.10 (s, 6H).

**4-(Pyren-1-yl)tpy-IrCl<sub>3</sub>.**—A yellow powder was obtained as the product (50 mg, 68%).  $^1\text{H NMR}$  (400 MHz, DMSO):  $\delta$  9.27 (dd,  $J = 5.6, 1.0$  Hz, 2H), 9.11 (s, 2H), 8.82 (d,  $J = 8.1$  Hz, 2H), 8.56 (d,  $J = 8.0$  Hz, 1H), 8.45–8.32 (m, 7H), 8.26 (td,  $J = 7.9, 1.6$  Hz, 2H), 8.18 (t,  $J = 7.6$  Hz, 1H), 8.02–7.97 (m, 2H).

### General Synthetic Procedure for Complexes Ir1–Ir6.

A degassed ethylene glycol suspension of 4-(4'-R-phenyl)tpy-IrCl<sub>3</sub> (0.1 mmol) (R = phenyl for **Ir1**, **Ir2**, **Ir4**, and **Ir6**; dimethylamino for **Ir3**; and pyren-1-yl for **Ir5**) and the other corresponding tpy-based ligand (0.1 mmol) was heated to 196 °C in dark for 1 h. After the mixture was cooled to room temperature, 10 mL aqueous  $\text{NH}_4\text{PF}_6$  (0.3 mmol) was added to precipitate out the crude product. The crude product was then purified by column chromatography on alumina gel. Dichloromethane and hexane (1:1, v/v) were used as the eluent first to remove the unreacted tpy ligands. Then, the mixed acetone/water eluent was used with a gradient of 100:0 to 95:5 (v/v) to obtain the target complexes.

**Ir1.**—A yellow powder was obtained as the product (80 mg, 64%).  $^1\text{H NMR}$  (400 MHz, DMSO):  $\delta$  9.62 (s, 4H), 9.22 (d,  $J = 8.1$  Hz, 4H), 8.52–8.41 (m, 4H), 8.38 (td,  $J = 8.0, 1.4$  Hz, 4H), 7.95 (d,  $J = 4.9$  Hz, 4H), 7.85 (t,  $J = 7.6$  Hz, 4H), 7.76 (t,  $J = 7.4$  Hz, 2H), 7.62–7.52 (m, 4H). ESI-HRMS ( $m/z$ , in acetonitrile): calcd for  $[\text{C}_{42}\text{H}_{30}\text{IrN}_6]^{3+}$ , 270.4055; found, 270.4060. Anal. Calcd (%) for  $\text{C}_{42}\text{H}_{30}\text{F}_{18}\text{IrN}_6\text{P}_3 \cdot 0.8\text{H}_2\text{O}$ : C, 40.03; H, 2.53; N, 6.67. Found: C, 40.39; H, 2.93; N, 7.06.

**Ir2.**—A red powder was obtained as the product (28 mg, 22%).  $^1\text{H NMR}$  (500 MHz, DMSO):  $\delta$  9.60 (s, 2H), 9.44 (s, 2H), 9.20 (dd,  $J = 7.7, 4.5$  Hz, 4H), 8.43 (t,  $J = 8.7$  Hz, 4H), 8.35 (dd,  $J = 16.3, 8.2$  Hz, 4H), 7.98 (d,  $J = 5.9$  Hz, 2H), 7.92 (d,  $J = 5.9$  Hz, 2H), 7.84 (t,  $J = 7.6$  Hz, 2H), 7.76 (t,  $J = 7.4$  Hz, 1H), 7.62–7.56 (m, 2H), 7.53 (t,  $J = 6.5$  Hz, 2H), 7.03 (d,  $J$

= 8.9 Hz, 2H), 3.18 (s, 6H). ESI-HRMS (*m/z*, in acetonitrile): calcd for  $[C_{44}H_{35}IrN_7]^{3+}$ , 284.7529; found, 284.7528. Anal. Calcd (%) for  $C_{44}H_{35}F_{18}IrN_7P_3$ : C, 41.00; H, 2.74; N, 7.61. Found: C, 40.64; H, 2.58; N, 7.61.

**Ir3.**—A red powder was obtained as the product (61 mg, 46%).  $^1H$  NMR (400 MHz, DMSO):  $\delta$  9.42 (s, 4H), 9.18 (d,  $J$  = 8.2 Hz, 4H), 8.41 (d,  $J$  = 9.2 Hz, 4H), 8.33 (td,  $J$  = 8.0, 1.4 Hz, 4H), 7.98–7.91 (m, 4H), 7.58–7.47 (m, 4H), 7.03 (d,  $J$  = 9.2 Hz, 4H), 3.18 (s, 12H). ESI-HRMS (*m/z*, in acetonitrile): calcd for  $[C_{46}H_{40}IrN_8]^{3+}$ , 299.1003; found, 299.1010. Anal. Calcd (%) for  $C_{46}H_{40}F_{18}IrN_8P_3 \cdot 4H_2O$ : C, 39.35; H, 3.45; N, 7.98. Found: C, 39.33; H, 3.48; N, 8.05.

**Ir4.**—A red powder was obtained as the product (118 mg, 86%).  $^1H$  NMR (400 MHz, DMSO):  $\delta$  9.68 (s, 2H), 9.65 (s, 2H), 9.30 (d,  $J$  = 8.2 Hz, 2H), 9.14 (d,  $J$  = 8.0 Hz, 2H), 8.73 (dd,  $J$  = 14.2, 8.6 Hz, 2H), 8.54–8.49 (m, 5H), 8.48–8.41 (m, 4H), 8.33 (dd,  $J$  = 12.6, 4.6 Hz, 2H), 8.26 (t,  $J$  = 7.6 Hz, 2H), 8.16 (d,  $J$  = 5.2 Hz, 2H), 8.02 (d,  $J$  = 5.7 Hz, 2H), 7.87 (t,  $J$  = 7.5 Hz, 2H), 7.78 (t,  $J$  = 7.4 Hz, 1H), 7.73–7.68 (m, 2H), 7.60 (dd,  $J$  = 10.5, 4.3 Hz, 2H). ESI-HRMS (*m/z*, in acetonitrile): calcd for  $[C_{52}H_{34}IrN_6]^{3+}$ , 311.7493; found, 311.7489. Anal. Calcd (%) for  $C_{52}H_{34}F_{18}IrN_6P_3 \cdot 1.2H_2O \cdot 0.6C_3H_6O$  ( $C_3H_6O$ : acetone): C, 45.30; H, 2.83; N, 5.89. Found: C, 45.52; H, 3.13; N, 6.14.

**Ir5.**—A red powder was obtained as the product (107 mg, 71%).  $^1H$  NMR (400 MHz, DMSO):  $\delta$  9.69 (s, 4H), 9.21 (d,  $J$  = 8.6 Hz, 4H), 8.80 (d,  $J$  = 9.4 Hz, 2H), 8.71 (d,  $J$  = 7.8 Hz, 2H), 8.60–8.57 (m, 2H), 8.50 (td,  $J$  = 12.1, 5.3 Hz, 10H), 8.42–8.35 (m, 6H), 8.25 (t,  $J$  = 7.7 Hz, 4H), 7.76–7.65 (m, 4H). ESI-HRMS (*m/z*, in acetonitrile): calcd for  $[C_{62}H_{38}IrN_6]^{3+}$ , 353.0931; found, 353.0924. Anal. Calcd (%) for  $C_{62}H_{38}F_{18}IrN_6P_3 \cdot 3H_2O \cdot 0.5C_6H_{14}$  ( $C_6H_{14}$ : hexane): C, 49.06; H, 3.23; N, 5.28. Found: C, 48.69; H, 3.50; N, 5.49.

**Ir6.**—A yellow powder was obtained as the product (74 mg, 53%).  $^1H$  NMR (400 MHz, DMSO):  $\delta$  9.62 (s, 2H), 9.57 (s, 2H), 9.22 (d,  $J$  = 8.3 Hz, 4H), 8.49 (d,  $J$  = 8.9 Hz, 2H), 8.45 (d,  $J$  = 7.4 Hz, 2H), 8.37 (t,  $J$  = 7.9 Hz, 4H), 8.02–7.90 (m, 4H), 7.85 (t,  $J$  = 7.6 Hz, 2H), 7.77 (t,  $J$  = 7.4 Hz, 1H), 7.57 (dd,  $J$  = 12.1, 4.5 Hz, 4H), 7.41 (d,  $J$  = 8.9 Hz, 2H), 4.50 (s, 3H), 4.35–4.32 (m, 2H), 3.88–3.85 (m, 2H), 3.69–3.66 (m, 2H), 3.62–3.58 (m, 2H), 3.58–3.55 (m, 2H), 3.49–3.46 (m, 2H). ESI-HRMS (*m/z*, in acetonitrile): calcd for  $[C_{49}H_{44}IrN_6O_4]^{3+}$ , 324.4352; found, 324.4362. Anal. Calcd (%) for  $C_{49}H_{44}F_{18}IrN_6O_4P_3 \cdot 4H_2O \cdot 2C_3H_6O \cdot 1.5CH_2Cl_2$  ( $C_3H_6O$ : acetone): C, 39.37; H, 3.92; N, 4.88. Found: C, 39.63; H, 3.92; N, 4.59. The solubility of this complex in  $H_2O$  is approximately 0.33 mg/mL.

### Photophysical Measurements.

The spectroscopic grade solvents used for the photophysical studies were purchased from Alfa Aesar. The UV–vis absorption spectra of complexes **Ir1–Ir6** were recorded on a Varian Cary 50 spectrophotometer, and the steady-state emission spectra were measured using a HORIBA FluoroMax-4 fluorometer/phosphorometer. The relative actinometry method was applied for determining the emission quantum yields for all complexes. Quinine bisulfate ( $\lambda_{ex}$  = 347.5 nm,  $\Phi_{em}$  = 0.546)<sup>52</sup> in 1N  $H_2SO_4$  solution was used as the reference for

complex **Ir1**, and the degassed acetonitrile solution of  $[\text{Ru}(\text{bpy})_3]\text{Cl}_2$  ( $\Phi_{\text{em}} = 0.097$ ,  $\lambda_{\text{ex}} = 436 \text{ nm}$ )<sup>53</sup> was used as the reference for complexes **Ir2–Ir6**. For all of the emission measurements, the sample solutions were degassed with  $\text{N}_2$  for 40 mins. prior to each measurement.

The nanosecond transient difference absorption (TA) measurements for complexes **Ir1–Ir6** in degassed acetonitrile solutions were carried out on an Edinburgh LP920 laser flash photolysis spectrometer. The third harmonic output (355 nm) from a Quantel Brilliant Nd:YAG laser (pulse duration = 4.1 ns; repetition rate = 1 Hz) was used as the excitation light. The singlet depletion method<sup>54</sup> was used for determining the triplet excited-state molar extinction coefficients ( $\epsilon_{\text{T}}$ ). Then, the relative actinometry<sup>55</sup> was applied for calculating the triplet excited-state quantum yields, with SiNc in benzene solution ( $\epsilon_{590 \text{ nm}} = 70,000 \text{ L mol}^{-1}\text{cm}^{-1}$ ,  $\Phi_{\text{T}} = 0.20$ )<sup>56</sup> being used as the reference.

### Singlet Oxygen Quantum Yield Measurement.

A PTI Quantamaster that is equipped with a Hamamatsu R5509–42 near-infrared (NIR) PMT was utilized to measure the singlet oxygen emission centered at 1268 nm from the 5  $\mu\text{M}$  air-saturated (with an oxygen concentration of 21%) acetonitrile solutions of complexes **Ir1–Ir6**. The relative actinometry was used to determine the singlet oxygen quantum yields ( $\Phi_{\Delta}$ ) of **Ir1–Ir6** with  $[\text{Ru}(\text{bpy})_3](\text{PF}_6)_2$  in aerated CH<sub>3</sub>CN ( $\Phi_{\Delta} = 0.56$ )<sup>57</sup> being used as the standard sample. The calculated  $\Phi_{\Delta}$  values were reproducible to within <5%.

### Computational Methodology.

The singlet ground state geometries for all complexes were optimized using the density functional theory (DFT),<sup>58</sup> as implemented in Gaussian16@ software package.<sup>59</sup> PBE1PBE functional<sup>60</sup> and the mixed basis set of LANL2DZ<sup>61</sup> for Ir and 6–31G\*<sup>62</sup> for other elements were used for all ground-state calculations. It is a common practice to employ an effective core potentials (ECPs) basis such as LANL2DZ for transition metals because ECPs are parameterized to implicitly account for scalar relativistic (SR) effects, which are known to be significant for Ir. The solvent effect was incorporated using the conductor-like polarizable continuum model (CPCM),<sup>63</sup> with acetonitrile dielectric constant being used as the solvent model to be consistent with the experimental condition.

Linear response time-dependent DFT (TDDFT)<sup>64</sup> was utilized to calculate optical transitions. For these calculations, we modified the PBE1PBE functional by increasing the Hartree-Fock (HF) exchange part to 32%, which provided a better agreement with the experimental spectra of **Ir1–Ir6**. The mixed LANL2DZ/6–31G\* basis set and CPCM/ acetonitrile solvent model were used for excited state calculations. The experimental UV-vis absorption spectra were simulated by calculating up to 70 optical transitions. Gaussian function with a broadening parameter of 0.12 eV was used to obtain thermal broadening of each transition to match the line shapes of the experimental absorption spectra.

Emission energies were calculated by optimizing the lowest triplet excited state using the analytical gradient TDDFT. The same functional and basis sets used for calculations of the absorption spectra were employed for the emission energy calculations. Natural transition

orbitals (NTOs)<sup>65</sup> were generated from the transition density matrices obtained from TDDFT calculations to demonstrate the nature of the electron-hole pairs contributing to each optical transition. All NTOs were visualized by VMD software<sup>66</sup> with a 0.02 isosurface. All calculation were carried out via Gaussian16@ software package.

### Photobiological Activity Studies.

The experimental details for cell culture, cytotoxicity/photocytotoxicity, confocal microscopy, and *in vitro* ROS generation on SK-MEL-28 cells; and the *in vitro* cytotoxicity/photocytotoxicity on human breast cancer (MCF-7) cells and the *in vivo* antitumor evaluation on female Balb/c nude mice bearing the MCF-7 xenograft tumors are provided in the Supporting Information.

It is worth noting that the PF<sub>6</sub><sup>-</sup> salts of the complexes were used for all of the photophysical studies and the singlet oxygen measurement; while the Cl<sup>-</sup> salts of the complexes were used for the photobiological activity studies for their better water solubility in aqueous solution.

## RESULTS AND DISCUSSION

### Electronic Absorption.

Figure 1 displays the UV–vis absorption spectra (experimental and calculated ones) of complexes **Ir1–Ir6** in acetonitrile solutions; and Table 1 lists the measured absorption band maxima and molar extinction coefficients. The corresponding experimental and calculated spectra were compared for each complex and the results are provided in the Supporting Information Figure S1.

The absorption followed the Beer's law in the concentration range ( $1 \times 10^{-6}$  to  $1 \times 10^{-4}$  mol·L<sup>-1</sup>) used in our study, indicating that no ground-state aggregation occurred in the tested concentration range. The spectra of all complexes share some common features: they all contain structured, high-energy absorption bands with large molar extinction coefficients at wavelengths <360 nm, and broad, featureless low-energy absorption band beyond this wavelength (for **Ir1** the low-energy band does not separate as clearly from the high-energy absorption bands as those in the other complexes). Based on the spectral features and the molar extinction coefficients, we tentatively attribute the high-energy absorption bands to predominant ligand-localized <sup>1</sup> $\pi, \pi^*$  transitions, while the low-energy broad band to predominant charge-transfer (<sup>1</sup>CT) transitions. These assignments are partially supported by the solvent-dependent absorption spectral study on these complexes. As shown in Figure S2, the high-energy bands were not sensitive to the polarity of solvent, but the low-energy band was. The different responses of the high-energy and low-energy absorption bands to the solvent polarity change were in accordance with their respective <sup>1</sup> $\pi, \pi^*$  and <sup>1</sup>CT nature of these bands.

It is apparent that the nature of the 4-Ar substituent(s) on tpy ligand impacted the energy of the low-energy absorption band dramatically. Complexes **Ir2** and **Ir3** that contain the strong electron-donating 4'-N(CH<sub>3</sub>)<sub>2</sub>Ph substituent drastically red-shifted the low-energy absorption band compared to that in **Ir1**; and the molar extinction coefficient of this band in **Ir3** is almost double that in **Ir2**. The similar phenomenon was observed in complexes **Ir4**



and **Ir5** bearing the  $\pi$ -donating pyren-1-yl substituent. In complex **Ir6**, the relatively weaker electron-donating 4'-CH<sub>3</sub>(OCH<sub>2</sub>CH<sub>2</sub>)<sub>3</sub>OPh substituent also induced a well-separated charge-transfer absorption band at 375 nm compared to that of **Ir1**, but the shift to longer wavelength is not as drastic as those in complexes **Ir2–Ir5**. The electron-donating substituents induced charge-transfer absorption band was reported in other bis(terpyridine) Ir(III) complexes containing 4'-NH<sub>2</sub>Ph or 4'-NMe<sub>2</sub>Ph<sub>2</sub> substituents.<sup>41,42</sup>

To unambiguously attribute the natures of the absorption bands, time-dependent density functional theory (TDDFT) calculations were conducted for complexes **Ir1–Ir6** in CH<sub>3</sub>CN. As Figure S1 in Supporting Information indicated, the calculated absorption spectra matched the experimental results quite well with respect to both the energies and the spectral features. The obtained natural transition orbitals (NTOs) contributing to the major transitions of the low-energy absorption band and the high-energy absorption bands are given in Table 2 and Supporting Information Table S2, respectively. As shown in Table 2, the lowest-energy transitions (S<sub>1</sub> state) for all complexes all possessed the intraligand charge transfer (<sup>1</sup>ILCT) / metal-to-ligand charge transfer (<sup>1</sup>MLCT) / <sup>1</sup> $\pi, \pi^*$  configurations. However, the <sup>1</sup>ILCT contribution increased in the S<sub>1</sub> states of **Ir2–Ir5** because of the increased electron-donating ability of the 4'-substituents in these complexes. In addition, ligand-to-ligand charge transfer (<sup>1</sup>LLCT) also made minor contribution to the low-energy absorption bands in these complexes. In contrast, the low-energy absorption band in **Ir1** had more <sup>1</sup> $\pi, \pi^*$  character due to the weaker electron-donating ability of the Ph substituent compared to the substituents in **Ir2–Ir6**. For the high-energy absorption bands in the regions of 280–370 nm, the NTOs in Tables S1 indicated predominant ligand centered <sup>1</sup> $\pi, \pi^*$  transitions, admixing with some charge transfer characters. Because of the strong intraligand charge-transfer nature of the low-energy absorption bands in **Ir2–Ir6**, the increased electron-donating ability of the 4-Ar substituent on tpy caused the significant red-shift of these absorption bands. The stronger of the electron donor, the more red-shift of this band.

### Photoluminescence.

The emission characteristics of complexes **Ir1–Ir6** were investigated at room temperature in a variety of solvents, including acetonitrile, tetrahydrofuran (with 1% acetonitrile), and dichloromethane (with 5% acetonitrile), and the normalized emission spectra in acetonitrile are displayed in Figure 2. A summary of the emission parameters, including the emission maxima ( $\lambda_{em}$ ), lifetimes ( $\tau_{em}$ ), and quantum yields ( $\Phi_{em}$ ), is provided in Tables 1 and S3. The emission of **Ir3** was too weak to be detected. Its emission spectrum and parameters are not included in Figure 2 and Tables 1 and S3.

All complexes except for **Ir3** were emissive at room temperature in fluid solutions, and the emission wavelengths were much red-shifted (3024 – 8713 cm<sup>-1</sup>) in comparison to their corresponding excitation wavelengths. Except for the short-wavelength shoulder at 577 nm in **Ir4**, the emission signals from **Ir1**, **Ir2**, and **Ir6** decayed relatively slowly, with a lifetime of several microseconds, and the emission was prone to oxygen quenching. All these characteristics imply a phosphorescence nature of the emission from these complexes. In addition to this phosphorescence band, **Ir4** possessed another emission band at 577 nm, which was not subject to oxygen quenching (Figure S4) and thus suggests fluorescence from

the singlet excited state. The lifetime monitored at this wavelength was too short to be accurately determined on our instrument ( $< 5$  ns), in line with the fluorescence nature of this emission band. The appearance of both fluorescence and phosphorescence emission has been reported for a 4-(pyren-1-yl)tpy Pt(II) complex<sup>67</sup> and for a dinuclear Pt(II) terpyridine complex bridged with a fluorenyl group.<sup>68</sup>

The emission spectrum of **Ir1** displayed a well-resolved vibronic structure with a minor solvatochromic effect (Figure S5). With reference to the other Ir(III) terpyridine complexes bearing alkylphenyl-substituted tpy ligand(s),<sup>40–42</sup> the emitting state of **Ir1** can be tentatively ascribed to predominant ph-tpy localized  $^3\pi, \pi^*$  state. However, the shorter lifetime and the less salient vibronic structure of **Ir1** in comparison to the emission from a pure  $^3\pi, \pi^*$  emitting state suggest that the emitting state of **Ir1** probably admixes some charge transfer configurations, likely the  $^3\text{MLCT}/^3\text{ILCT}$  configurations. In contrast to **Ir1**, the phosphorescence spectra of **Ir2** and **Ir6** were broad and lacked of vibronic structures, and the solvatochromic effects were more obvious. Moreover, the emission quantum yields of these two complexes became much smaller. These characteristics imply the involvement of more charge transfer characters in their emitting states. Considering the electron-donating nature of the dimethylamino and the oligoether groups on the ph-tpy frame in **Ir2** and **Ir6**,  $^3\text{ILCT}$  could play a major role in the emitting triplet excited states. The involvement of the  $^3\text{ILCT}$  character caused the red-shifts of the emission bands and lowered the emission quantum yields because of the increased non-radiative decay rate that is intrinsically associated with the charge-transfer configuration. Note that, **Ir3** bearing two dimethylamino substituents on the ph-tpy ligands could have even more charge transfer character in its emitting state, leading to an extremely weak luminescence that could not be detected. Due to the stronger electron-donating ability of the dimethylamino substituent than that of the oligoether group, stronger  $^3\text{ILCT}$  would present in **Ir2** than in **Ir6**. Consequently, **Ir2** exhibited a more red-shifted emission with a much lower quantum yield in comparison to those of **Ir6**.

Considering the phosphorescence in **Ir4** and **Ir5**, although the spectra were featureless and much red-shifted, and the emission signals were too weak to allow for the emission lifetimes to be determined (which all resembled the emission characteristics of **Ir2** and **Ir6**), the emission energies were much less sensitive to the solvent polarity (which was similar to that of **Ir1**). Therefore, the emitting states in these two complexes might not involve much charge transfer configuration. In view of the similar emission energy of these two complexes to those of other reported transition metal complexes containing pyrenyl-containing ligand,<sup>67,69–71</sup> we tentatively attribute the observed phosphorescence from these two complexes to pyrene-localized  $^3\pi, \pi^*$  state.

The analytical TDDFT calculations on the lowest triplet excited states ( $T_1$ ) of these complexes supported our aforementioned attributions to the nature of the emission. As shown in Table 3, the NTOs clearly revealed that the  $T_1$  state of **Ir1** was dominated by the  $^3\pi, \pi^*$  configuration, admixing with some  $^3\text{MLCT}/^3\text{ILCT}/^3\text{LMCT}$  configurations; whereas the  $T_1$  states of **Ir2** and **Ir6** had increased  $^3\text{ILCT}$  contributions along with the  $^3\pi, \pi^*/^3\text{MLCT}/^3\text{LMCT}$  configurations. In contrast, the holes of the  $T_1$  states of **Ir4** and **Ir5** were exclusively on the pyrene motifs, while the electrons were delocalized to the central pyridine

ring and very little to the d orbital of the Ir(III) ion. Therefore, the emitting  $T_1$  states in **Ir4** and **Ir5** have almost exclusively pyrene-based  $^3\pi,\pi^*$  character, admixing with very minor  $^3\text{ILCT}/^3\text{LMCT}$ .

### Transient Absorption (TA).

To further understand the triplet excited state characteristics of complexes **Ir1–Ir6**, especially for those complexes that do not emit or are weakly emissive, the nanosecond TA of these complexes was investigated in nitrogen purged acetonitrile solutions. Figure 3 shows the TA spectra of **Ir1–Ir6** at zero-delay after 355 nm excitation. The time-resolved spectra for each complex are provided in Figure S6 of the Supporting Information. The TA parameters, such as the TA band maxima and the triplet excited-state lifetimes by monitoring the decay of TA signals, are summarized in Table 1.

The deduced TA lifetimes of **Ir1** and **Ir6** are similar to their emission lifetimes in acetonitrile, implying that the transient absorbing excited states in these two complexes are the emitting states. Probably due to the increased  $^3\text{ILCT}$  contribution to the  $T_1$  state of **Ir6**, its TA band maximum was much red-shifted compared to that of **Ir1**, accompanied by the appearance of clear bleaching at the wavelength that was in accordance with its  $^1\text{ILCT}/^1\pi,\pi^*$  absorption band. For **Ir2**, its TA signal consisted of two components with distinct decay kinetics: the fast decayed signal had a lifetime of 9 ns and the slow one had a lifetime of 3.12  $\mu\text{s}$ , which was consistent with its emission lifetime. For **Ir3**, its TA signals were stronger than those in **Ir2** but decayed with a lifetime (8 ns) similar to that of the fast component in **Ir2**. The fast decayed TA spectrum of **Ir2** was quite similar to that of **Ir3**, with the similar TA band maxima and the similar bleaching occurring at their corresponding  $^1\text{ILCT}/^1\pi,\pi^*$  absorption bands. Thus, we preassembly assign these TA to predominant  $^3\text{ILCT}$  states. In contrast, the slower decayed TA spectral feature of **Ir2** resembled that of **Ir1**. In view of the similar lifetime of this long-lived TA species to its emission lifetime, we ascribe the slower TA component emanating from the  $^3\text{ILCT}/^3\pi,\pi^*/^3\text{MLCT}/^3\text{LMCT}$   $T_1$  state of **Ir2**. The observation of the rapid conversion of the short-lived transient species to the long-lived species in **Ir2** implies that the high-lying  $^3\text{ILCT}$  state was populated first then it decayed to the long-lived  $T_1$  state. The TA spectra of **Ir4** and **Ir5** resembled each other with long lifetimes, suggesting that the similar origin of the transient absorbing states. Considering the same nature of the  $T_1$  states in these two complexes and the similar TA spectral feature to that reported for a Pt(II) complex bearing pyrenyl-acetylide ligand,<sup>71</sup> we attribute the observed TA to the pyrenyl-localized  $^3\pi,\pi^*$  states. It is noted that the TA lifetime of **Ir5** is almost 1 order of magnitude longer than that of **Ir4** although their  $T_1$  states are both localized on the pyrenyl component. A careful examination of the NTOs in Table 3 for the  $T_1$  states of **Ir4** and **Ir5** revealed that **Ir4** contains slightly more  $^3\text{ILCT}$  character in its  $T_1$  state. The slightly more charge transfer character in the  $T_1$  state of **Ir4** may reduce its  $T_1$  lifetime. Alternatively, the dual emission of **Ir4** implies that the fluorescent  $^1\text{CT}$  state lies in proximity of the  $T_1$  state, which hypothetically allows for the coupling between these two states but does not reach an equilibrium. Consequently, the  $T_1$  lifetime of **Ir4** was reduced.

### Singlet Oxygen Generation.

Singlet oxygen generation is an important property for photobiological applications such as PDT that rely on cytotoxic ROS. Therefore, the singlet oxygen quantum yields ( $\Phi_{\Delta}$ ) were evaluated for **Ir1-Ir6**. These measurements were carried out in CH<sub>3</sub>CN relative to [Ru(bpy)<sub>3</sub>](PF<sub>6</sub>)<sub>2</sub> as the standard ( $\Phi_{\Delta}$ =56%)<sup>57</sup> using the inherent luminescence of <sup>1</sup>O<sub>2</sub> centered at approximately 1270 nm. The reason that  $\Phi_{\Delta}$  was measured in CH<sub>3</sub>CN as the solvent (rather than water or aqueous solutions) is because water quenches the emission from <sup>1</sup>O<sub>2</sub>, precluding the accurate determination of  $\Phi_{\Delta}$ .<sup>72</sup> In addition, pure water is not representative of a real biological environment, where it is expected that the complexes would be associated with biological macromolecules and thus experience greater hydrophobicity as a result. Although  $\Phi_{\Delta}$  in the real biological environment cannot be known with certainty, the measurement in CH<sub>3</sub>CN allows us to assess the potential of the complexes for producing <sup>1</sup>O<sub>2</sub> and compare this ability with other complexes in the literature, which are routinely reported in CH<sub>3</sub>CN.

Excitation spectra were collected for **Ir1-Ir6** with  $\lambda_{em}$ =1268 nm, and the excitation maxima were used as the excitation wavelengths in the emission measurement. The values for  $\Phi_{\Delta}$  using the corresponding excitation maximum for each compound are listed in Table 1. In this way,  $\Phi_{\Delta}$  represents the maximum efficiency for <sup>1</sup>O<sub>2</sub> generation in CH<sub>3</sub>CN provided the most effective excitation wavelength is used. In actual photobiological assays, however, broadband visible light was used. Generally speaking, the excitation maxima for <sup>1</sup>O<sub>2</sub> emission positively correlated with the longest wavelength maximum in the absorption spectra, with **Ir2** and **Ir3** generating more <sup>1</sup>O<sub>2</sub> with longer excitation wavelengths (>450 nm), **Ir1** and **Ir6** requiring shorter wavelengths (< 400 nm), and **Ir4** and **Ir5** intermediate at approximately 450 nm.

Within this small family of compounds, changes in the R-tpy groups had marked effects on <sup>1</sup>O<sub>2</sub> yields and proved to be a facile way to tune this parameter and better understand the nature of the excited states involved. The <sup>1</sup>O<sub>2</sub> quantum yields were largest for the pyrenyl-containing complexes **Ir4** and **Ir5**, with one pyrenyl group in **Ir4** being slightly more effective than two in **Ir5** (81% versus 75%). The dimethylaminophenyl substituents had detrimental effects on  $\Phi_{\Delta}$ , whereby **Ir2** and **Ir3** were less than 1%, and even R<sub>1</sub>=R<sub>2</sub>=Ph (**Ir1**) showed marked attenuation ( $\Phi_{\Delta}$  = 14%). Interestingly, when one Ph group in **Ir1** was replaced with the water-solubilizing polyether substituent in **Ir6**, the <sup>1</sup>O<sub>2</sub> quantum yield increased four-fold. The pyrenyl group is known to have an effective triplet state of  $\pi, \pi^*$  character for generating <sup>1</sup>O<sub>2</sub> so the large values for  $\Phi_{\Delta}$  with **Ir4** and **Ir5** were in line with expectations and justified the use of these groups as substituents despite their hydrophobicities. The relatively large <sup>1</sup>O<sub>2</sub> quantum yields for **Ir4** and **Ir5** positioned these compounds as potentially good photobiological agents.

### Cytotoxicity and Photocytotoxicity toward Human Melanoma (SK-MEL-28) Cancer Cells.

The six complexes of this family were explored for their cytotoxicities and photobiological activities using the SK-MEL-28 human skin melanoma cancer cell line (Figure 4). Briefly, cells were dosed with the complex in the range of 1 nM to 300  $\mu$ M and incubated at 37 °C (5% CO<sub>2</sub>) for approximately 16 h before receiving a dark or light treatment. Excess PS was

not removed before delivering the light treatment in order to capture any photoactivated uptake that may occur.

The light treatments were either broadband visible light of  $100 \text{ J cm}^{-2}$  or monochromatic red light (625 nm) of the same fluence. The cells were incubated again following the dark or light treatment and quantified with the resazurin cell viability dye at 48 h.<sup>73</sup> Cytotoxicity and photocytotoxicities are reported in Table 4 as the effective concentration of complex to reduce cell viability to 50%,  $\text{EC}_{50}$ , in this assay, and the phototherapeutic indices (PIs) are the ratios of the dark to light  $\text{EC}_{50}$  values and represent the amplification of cytotoxicity with the light treatment.

**Ir1-Ir4** were nontoxic to cells over the concentration range tested, and thus  $\text{EC}_{50}$  values were estimated as  $>300 \mu\text{M}$ , with precise determination limited by the insolubilities of the complexes in the assay media at higher concentrations. **Ir5** was slightly more toxic than **Ir1-Ir4** but relatively nontoxic overall with an  $\text{EC}_{50}$  greater than  $100 \mu\text{M}$ . Interestingly, **Ir6** was cytotoxic without a light treatment ( $\text{EC}_{50} = \sim 7 \mu\text{M}$ ), underscoring that the polyethoxy substituent that was incorporated to enhance aqueous solubility resulted in high baseline cytotoxicity and would limit the utility of the complex as a photobiological agent despite a  $^1\text{O}_2$  quantum yield of almost 60%. The origin of this cytotoxicity was not investigated further as part of the present study.

All of the complexes exhibited enhanced cytotoxicity with visible light, albeit to significantly different degrees. The two- to four-fold enhancement for **Ir1-Ir2** and **Ir6** was not large enough to qualify these complexes for further study as photobiological agents. Likewise, the modest PI of  $>21$  and the low photocytotoxicity ( $\text{EC}_{50} = \sim 14 \mu\text{M}$ ) of **Ir3** were not notable. However, the pyrenyl-containing complexes **Ir4** and **Ir5** had submicromolar  $\text{EC}_{50}$  values that were similar (180 and 200 nM, respectively) and large PIs. **Ir4** that was nontoxic in the dark had the largest PI of the series at  $>1657$ , which positively correlated with its  $^1\text{O}_2$  quantum yield (Figure 5). The slightly higher dark cytotoxicity of **Ir5** led to a reduced PI of 628, but this number is still considered quite large relative to most PDT agents.

While **Ir4** and **Ir5** had very slight enhancements of their cytotoxicities with 625-nm light (PIs on the order of 2–3), none of the complexes could be considered as PDT agents with red light. Therefore, the very high potencies with visible light are presumably due to the shorter wavelengths in the visible spectrum, and thus these complexes would be best suited for applications requiring superficial activation of PSs with blue or green light. The potent *in vitro* photobiological effects of **Ir4** and **Ir5**, the pyrenyl-based complexes of the series, further illustrate the utility of highly photosensitizing  $^3\pi, \pi^*$  states that have been previously documented for PDT.<sup>5</sup>

Cells treated with **Ir4** and **Ir5** at  $50 \mu\text{M}$  were observed by laser scanning confocal microscopy after a dark or a visible light treatment of  $50 \text{ J cm}^{-2}$  (Figure 6). The light condition was chosen such that enough cells remained for viewing. The inherent luminescence from **Ir4** was visible in the cytosol of the dark-treated cells, and the dead/dying cells and cellular debris remaining after light treatment was highly luminescent. Even

in the dark, cells treated with **Ir4** underwent morphological changes from elongated and spindle-shaped to detached and spherical. Under the same treatment conditions, **Ir5** appeared to be taken up by cells in the dark less readily based on luminescence as an indicator. The cells dosed with **Ir5** and treated with visible light, however, displayed bright luminescence from the cytosol with accumulation possibly in the mitochondria. Treatment of cells with **Ir5** under both dark and light conditions resulted in few morphological changes at the observation time point. It is interesting to note that the cells appeared healthier upon treatment with **Ir5** despite the higher dark toxicity measured in the dose-response assay for this complex.

The confocal experiments cannot definitively establish cellular localization since the experiment relies on luminescence from the complex, which in turn is dependent on environment, but they do highlight the potential of the complexes to act as theranostic agents despite emission quantum yields of <1% in cell-free conditions. The number of pyrenyl units incorporated into the Ir(R-tpy)<sub>2</sub><sup>3+</sup> scaffold appears to influence uptake, localization, and cellular responses, and consequently cytotoxicity and photocytotoxicity. However, the observations in the confocal experiments did not have a clear correlation with the dose-response outcomes given that **Ir5** was slightly more cytotoxic with a smaller PI in the dose-response assays.

#### **In Vitro ROS Detection in Treated Human Melanoma (SK-MEL-28) Cancer Cells.**

The photobiological activities associated with the complexes, notably **Ir4** and **Ir5**, were attributed to ROS generation, specifically <sup>1</sup>O<sub>2</sub>. As expected, the photocytotoxicities toward SK-MEL-28 cells correlated well with values measured for  $\Phi_{\Delta}$  under cell-free conditions. However, other ROS could also be involved (*e.g.*, superoxide anion, hydrogen peroxide, hydroxyl radical) so the highly sensitive 2',7'-dichlorodihydrofluorescein diacetate (DCFDA) fluorophore<sup>74</sup> was used as a general probe for reporting on ROS production in live cells (Figure 7). This assay is based on the cell permeable DCFDA being deacetylated by cellular esterases to its nonfluorescent analog, which reacts with ROS to yield the oxidized DCF product that is highly fluorescent.

To probe for ROS production by **Ir1-Ir6** in the dark and with visible light activation, SK-MEL-28 cells were pre-incubated with DCFDA and then subjected to the assay described for (photo)cytotoxicity except that a sub-lethal light treatment was used to ensure a proportion of live cells for intracellular ROS quantification. Fluorescence from DCF was markedly enhanced with visible light treatment for all of the complexes. The complex that produced the maximum fluorescence from DCF was **Ir2**, which had the smallest <sup>1</sup>O<sub>2</sub> quantum yield of the series and one of the largest EC<sub>50</sub> values (corresponding to lowest photobiological activity). However, these maximal values occurred at a very high concentration of PS (>300  $\mu$ M). It is more informative to compare the onset of ROS production among the complexes, whereby **Ir4** and **Ir5** produce the onset of DCF fluorescence at the lowest concentrations. For example, at 5  $\mu$ M and 10  $\mu$ M, **Ir4** and **Ir5** clearly induced more DCF fluorescence than the other complexes. The onset of DCF fluorescence is important because once cells begin to die, the DCF fluorescence decreases. Consequently, the concentration at which maximal DCF fluorescence is observed for a

compound (rather than the maximum value itself) is also informative. The earlier this occurs, the more potent the PS in terms of ROS production. For **Ir4** and **Ir5**, it occurs at 50  $\mu\text{M}$  with decreases thereafter. **Ir6** is the only other complex in the series that has a similar onset (maximal at 50  $\mu\text{M}$ ) of DCF fluorescence. However, its dark cytotoxicity negates any enhanced toxicity that might be gained through photosensitized ROS production.

The intracellular ROS assay also points toward **Ir4** and **Ir5** as being the most potent PSs of the series, underscoring the importance of the pyrenyl units to the photobiological activities of this class complexes. The agreement between the cell-free  $^1\text{O}_2$  quantum yields and the onset of detectable *in vitro* ROS production points toward cytotoxic  $^1\text{O}_2$  as perhaps the most important ROS mediator, and suggests PDT as the underlying mechanism.

### ***In Vitro* and *In Vivo* PDT Studies Using Human Breast (MCF-7) Cancer Cells and Tumor Xenografts.**

The promising *in vitro* photobiological activity of **Ir4** toward SK-MEL-28 cells, specifically the strong PDT effect, warranted further investigation. To probe the robustness of the response, we tested its effectiveness toward a different cell line with a different light source and protocol. Further, we tested this response in the more clinically relevant mouse xenograft model. Blue light (450 nm, 50 or 100  $\text{mW cm}^{-2}$ ) was used because the lowest-energy absorption band of **Ir4** occurred at 440 nm, and thus that is where the maximum response might be expected. We wish to show proof-of-concept and recognize that clinical applications would mostly likely require longer wavelengths and possibly optimized structures.

The PDT effects of **Ir4** toward the MCF-7 breast cancer cell line and on the corresponding MCF-7 xenografts implanted on the Balb/c nude mice (16–18 g) were investigated. Figure 8a shows the cell viability comparison with and without light treatment upon incubation with increasing doses of **Ir4**. There was no dark toxicity over the tested concentration range, however, cells treated with **Ir4** and irradiated with 450-nm light (50  $\text{mW cm}^{-2}$ ) for 5 mins (15  $\text{J cm}^{-2}$ ) were destroyed in a dose-dependent manner. Notably, the cell viability decreased to approximately 5% with only 5 mins of irradiation at low micromolar concentrations of **Ir4**. The  $\text{EC}_{50}$  value against MCF-7 cells using this light condition was as low as 0.092  $\mu\text{M}$ .

We next tested whether **Ir4** and blue light could be effective for treating solid tumors with PDT in a mouse model. MCF-7 cells were implanted in the right flank of female Balb/c nude mice (16–18 g) to establish the xenograft solid tumors. When the tumor size reached 100–150  $\text{mm}^3$ , the mice were randomly divided into four groups with three mice in each group before the experiment, *i.e.* the control group without any treatment (control dark), the control group only with blue light irradiation (control light), the treatment group only with **Ir4** injection (**Ir4** dark), and the PDT treatment group with **Ir4** injection and blue light activation (**Ir4** light). **Ir4** was injected directly into the tumor (10  $\text{mg kg}^{-1}$ , 100  $\mu\text{L}$ ) in PET (6% polyethylene glycol 400, 3% ethanol, 1% Tween 80 and 90% PBS) for the two treatment groups. For the PDT treatment, one hour after the injection, the blue light (450 nm, 100  $\text{mW cm}^{-2}$ ) was delivered to the tumor site for 10 mins (60  $\text{J cm}^{-2}$ ).

The tumor volume and weight of the mice were monitored every two days, and the data for the 12-day post treatment period are provided in Figure 8b and 8c. The tumor weight comparison to the control groups at 12 days post treatment is provided in Figure 8d, and the separated solid tumors and the whole body images are shown in Figure 8e and 8f. Figures 8b–f demonstrate a measurable *in vivo* PDT effect on the MCF-7 xenograft tumors.

Tumors growth was dramatically inhibited, with essentially no change in tumor volume 12 days after the PDT treatment and tumor weight limited to approximately 10% compared to the control group that did not receive **Ir4** or a light treatment. The PDT treatment had almost no impact on the body weight gain of the mice, reflected by the similar body weight of the PDT treatment group with respect to the three control groups (Figure 8c). In fact, the slight increase in body weight for the control and treatment groups highlights the low dark toxicity of **Ir4**, the good tolerance of PDT, and the negligible side effects of the treatment.

## CONCLUSIONS

We presented the synthesis, photophysics, and photobiological studies of a series of tricationic mononuclear homoleptic or heteroleptic bis(terpyridine) Ir(III) complexes with various substituents at the 4-position of tpy. Compared to the parent complex (**Ir1**), the low energy absorption bands for the rest of complexes were gradually red-shifted, which are directly controlled by the different electron-donating abilities of the substituents. The stronger donors also stabilized the triplet emitting states and resulted in much weaker phosphorescence owing to the accelerated nonradiative decay rate. All complexes, except for **Ir3**, exhibited broad positive absorption bands in the visible and extending to the NIR region. The long-lived transient species in complexes **Ir4** and **Ir5** had a lifetime of ca. 5.8 and 24  $\mu$ s, respectively, which makes them suitable candidates for PDT study.

In fact, the complexes with the longest TA lifetimes (**Ir4** and **Ir5**) were also the strongest  $^1\text{O}_2$  generators under cell-free conditions, exhibited the most potent photobiological activities toward SK-MEL-28 cells, and appeared to be the most effective ROS producers *in vitro*. The pyrenyl group is clearly an important substituent for eliciting potent *in vitro* PDT effects, presumably due to the increased  $^3\pi, \pi^*$  character of the lowest-lying triplet excited states, which is known to prolong excited state lifetimes. Notably, the lifetime of the  $^3\pi, \pi^*$  state in **Ir4** is about ten times shorter than that for **Ir5**, possibly due to increased  $^3\text{ILCT}$  character and/or coupling to  $^1\text{CT}$  states of similar energy. Nevertheless, **Ir4** had the largest PI and was more than two-fold greater than that for **Ir5** due to its reduced dark cytotoxicity. The PI of >1657 is the strongest antiproliferative activity so far among the reported visible-light stimulated Ir(III) complexes. **Ir4** also exhibited a very strong *in vitro* PDT effect toward MCF-7 breast cancer cells and dramatically inhibited the xenograft tumor growth upon 450-nm light activation with essentially no dark toxicity and negligible side effects upon PDT treatment. Importantly, activity with **Ir4** was demonstrated using different light sources between two laboratories across two different cell lines as well as a tumor xenograft model, further validating our findings. These results demonstrate the potential of **Ir4**, and possible other Ir(III) bis(terpyridine) complexes, as PDT agents.



## Supplementary Material

Refer to Web version on PubMed Central for supplementary material.

## ACKNOWLEDGMENTS

W. Sun and S. Kilina acknowledge the financial support from the National Science Foundation (DMR-1411086 and CHE-1800476) for complex synthesis, characterization and computational simulation of the optical spectra. S. Kilina is grateful to the US Department of Energy (DE-SC008446) for financial support and Center for Computationally Assisted Science and Technology (CCAST) at the North Dakota State University and the National Energy Research Scientific Computing Center (NERSC) allocation Award No. 86678 (supported by the Office of Science of the Department of Energy under Contract No. DE-AC02-05CH11231) for computer access and administrative support. The photobiological studies on the SK-MEL-28 cells reported in this publication was supported by the National Cancer Institute of the National Institutes of Health under Award Number R01CA222227 to S. A. McFarland. The content is solely the responsibility of the authors and does not necessarily represent the official views of the National Institutes of Health. S. A. McFarland also acknowledges financial support from the University of North Carolina at Greensboro, the Natural Sciences and Engineering Council of Canada, and Acadia University. J. Tian thanks the National Natural Science Foundation of China (Grants 21601140 and 21871214) for supporting his part of the work on the breast cancer cells and xenograft tumor model. We also thank Wan Xu in Sun's group at NDSU for her help in checking some of the photophysical data that are not included in this paper.

## References

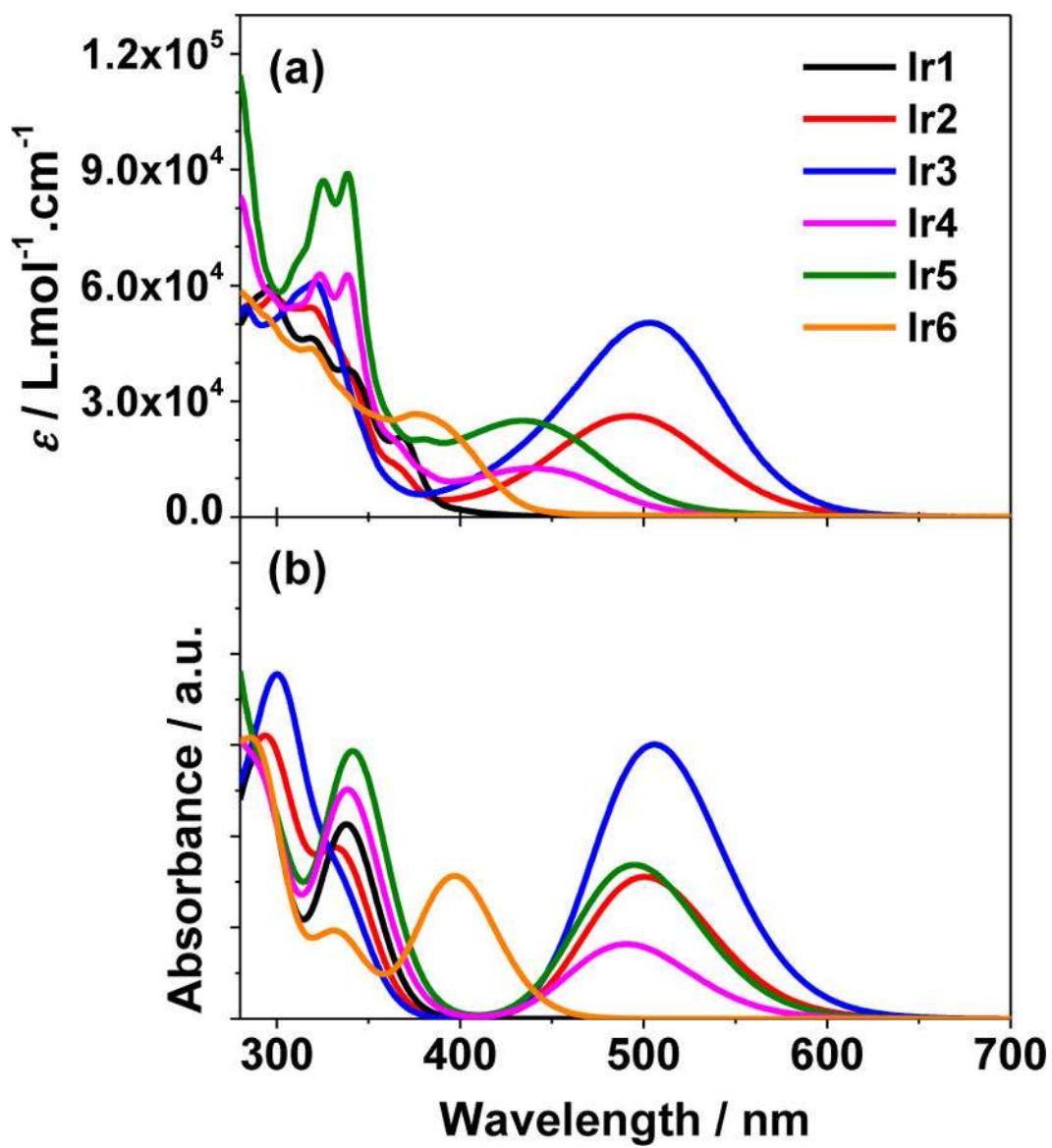
- (1). Celli JP; Spring BQ; Rizvi I; Evans CL; Samkoe KS; Verma S; Pogue BW; Hasan T Imaging and Photodynamic Therapy: Mechanisms, Monitoring, and Optimization. *Chem. Rev* 2010, 110, 2795–2838. [PubMed: 20353192]
- (2). Shi G; Monro S; Hennigar R; Colpitts J; Fong J; Kasimova K; Yin H; DeCoste R; Spencer C; Chamberlain L; Mandel A; Liljec L; McFarland SA Ru(II) Dyads Derived from  $\alpha$ -Oligothiophenes: A New Class of Potent and Versatile Photosensitizers for PDT. *Coord. Chem. Rev* 2015, 282–283, 127–138.
- (3). Li X; Lee S; Yoon J Supramolecular Photosensitizers Rejuvenate Photodynamic Therapy. *Chem. Soc. Rev* 2018, 47, 1174–1188. [PubMed: 29334090]
- (4). Wilson BC; Patterson MS The Physics, Biophysics and Technology of Photodynamic Therapy. *Phys. Med. Biol* 2008, 53, R61–R109. [PubMed: 18401068]
- (5). Monro S; Colón KL; Yin H; Roque J; Konda P; Gujar S; Thummel RP; Lilje L; Cameron CG; McFarland SA Transition Metal Complexes and Photodynamic Therapy from a Tumor-Centered Approach: Challenges, Opportunities, and Highlights from the Development of TLD1433. *Chem. Rev* 2019, 119, 797–828. [PubMed: 30295467]
- (6). Bellnier D. a; Dougherty TJ A Preliminary Pharmacokinetic Study of Intravenous Photofrin in Patients. *J. Clin. Laser Med. Surg* 1996, 14, 311–314. [PubMed: 9612197]
- (7). Allison RR; Sibata CH Oncologic Photodynamic Therapy Photosensitizers: A Clinical Review. *Photodiagnosis Photodyn. Ther* 2010, 7, 61–75. [PubMed: 20510301]
- (8). Dolmans DEJGJ; Fukumura D; Jain RK Photodynamic Therapy for Cancer. *Nat. Rev. Cancer* 2003, 3, 380–387. [PubMed: 12724736]
- (9). Gomer CJ; Razum NJ Acute Skin Response in Albino Mice Following Porphyrin Photosensitization Under Oxic and Anoxic Conditions. *Photochem. Photobiol* 1984, 40, 435–439. [PubMed: 6239295]
- (10). Abrahamse H; Hamblin MR New Photosensitizers for Photodynamic Therapy. *Biochem. J* 2016, 473, 347–364. [PubMed: 26862179]
- (11). Zhang J; Jiang C; FigueiróLongo JP; Azevedo RB; Zhang H; Muehlmann LA An Updated Overview on the Development of New Photosensitizers for Anticancer Photodynamic Therapy. *Acta Pharm. Sin. B* 2018, 8, 137–146. [PubMed: 29719775]
- (12). Sternberg ED; Dolphin D Second Generation Photodynamic Agents: A Review. *J. Clin. Laser Med. Surg* 1993, 11, 233–241. [PubMed: 10146514]

- (13). Kataoka H; Nishie H; Hayashi N; Tanaka M; Nomoto A; Yano S; Joh T New Photodynamic Therapy with Next-Generation Photosensitizers. *Ann. Transl. Med* 2017, 5, 183. [PubMed: 28616398]
- (14). Ormond AB; Freeman HS Dye Sensitizers for Photodynamic Therapy. *Materials* 2013, 6, 817–840. [PubMed: 28809342]
- (15). Bagchi D; Bhattacharya A; Dutta T; Nag S; Wulferding D; Lemmens P; Pal SK Nano MOF Entrapping Hydrophobic Photosensitizer for Dual-Stimuli-Responsive Unprecedented Therapeutic Action against Drug-Resistant Bacteria. *ACS Appl. Bio Mater* 2019, 2, 1772–1780.
- (16). Mari C; Pierroz V; Ferrari S; Gasser G Combination of Ru(II) Complexes and Light: New Frontiers in Cancer Therapy. *Chem. Sci* 2015, 6, 2660–2686. [PubMed: 29308166]
- (17). Zamora A; Viguera G; Rodríguez V; Santana MD, Ruiz J Cyclometalated Iridium(III) Luminescent Complexes in Therapy and Phototherapy. *Coord. Chem. Rev* 2018, 360, 34–76.
- (18). Stacey OJ; Pope SJ A. New Avenues in the Design and Potential Application of Metal Complexes for Photodynamic Therapy. *RSC Adv* 2013, 3, 25550–25564.
- (19). Jiang X; Zhu N; Zhao D; Ma Y New Cyclometalated Transition-Metal Based Photosensitizers for Singlet Oxygen Generation and Photodynamic Therapy. *Sci. China Chem* 2016, 59, 40–52.
- (20). Wang C; Lystrom L; Yin H; Hetu M; Kilina S; McFarland SA; Sun W Increasing the Triplet Lifetime and Extending the Ground-State Absorption of Biscyclometalated Ir(III) Complexes for Reverse Saturable Absorption and Photodynamic Therapy Applications. *Dalton Trans* 2016, 45, 16366–16378. [PubMed: 27711764]
- (21). Li Y; Tan CP; Zhang W; He L; Ji LN; Mao ZW Phosphorescent Iridium(III)-Bis-N-Heterocyclic Carbene Complexes as Mitochondria-Targeted Theranostic and Photodynamic Anticancer Agents. *Biomaterials* 2015, 39, 95–104. [PubMed: 25477176]
- (22). Majumdar P; Yuan X; Li S; Le Guennic B; Ma J; Zhang C; Jacquemin D; Zhao J Cyclometalated Ir(III) Complexes with Styryl-BODIPY Ligands Showing Near IR Absorption/Emission: Preparation, Study of Photophysical Properties and Application as Photodynamic/Luminescence Imaging Materials. *J. Mater. Chem. B* 2014, 2, 2838–2854.
- (23). Chen Y; Guan R; Zhang C; Huang J; Ji L; Chao H Two-Photon Luminescent Metal Complexes for Bioimaging and Cancer Phototherapy. *Coord. Chem. Rev* 2016, 310, 16–40.
- (24). Lo KK-W; Zhang KY Iridium(III) Complexes as Therapeutic and Bioimaging Reagents for Cellular Applications. *RSC Adv* 2012, 2, 12069–12083.
- (25). He L; Li Y; Tan C-P; Ye R-R; Chen M-H; Cao J-J; Ji L-N; Mao Z-W Cyclometalated Iridium(III) Complexes as Lysosome-targeted Photodynamic Anticancer and Real-time Tracking Agents. *Chem. Sci* 2015, 6, 5409–5418. [PubMed: 29861886]
- (26). Liu S; Liang H; Zhang KY; Zhao Q; Zhou X; Xu W; Huang WA Multifunctional Phosphorescent Iridium(III) Complex for Specific Nuclear Staining and Hypoxia Monitoring. *Chem. Commun* 2015, 51, 7943–7946.
- (27). Zhang G; Zhang H; Gao Y; Tao R; Xin L; Yi J; Li F; Liu W; Qiao J Near-Infrared-Emitting Iridium(III) Complexes as Phosphorescent Dyes for Live Cell Imaging. *Organometallics* 2014, 33, 61–68.
- (28). Lv W; Zhang Z; Zhang KY; Zhang Y; Yang H; Liu S; Xu A; Guo S; Zhao Q; Huang W A Mitochondria-Targeted Photosensitizer Showing Improved Photodynamic Therapy Effects under Hypoxia. *Angew. Chem. Int. Ed* 2016, 55, 9947–9951.
- (29). Li SP-Y; Lau CT-S; Louie M-W; Lam Y-W; Cheng SH; Lo KK-W Mitochondria-targeting Cyclometalated Iridium(III)-PEG Complexes with Tunable Photodynamic Activity. *Biomaterials* 2013, 34, 7519–7532. [PubMed: 23849346]
- (30). Qiu K; Ouyang M; Liu Y; Huang H; Liu C; Chen Y; Ji L; Chao H Two-photon Photodynamic Abalation of Tumor Cells by Mitochondria-targeted Iridium(III) Complexes in Aggregated States. *J. Mater. Chem. B* 2017, 5, 5488–5498.
- (31). Ouyang M; Zeng L; Qiu K; Chen Y; Ji L; Chao H Cyclometalated Ir<sup>III</sup> Complexes as Mitochondria-Targeted Photodynamic Anticancer Agents. *Eur. J. Inorg. Chem* 2017, 1764–1771.
- (32). Zheng Y; He L; Zhang D-Y; Tan C-P; Ji L-N; Mao Z-W Mixed-ligand Iridium(III) Complexes as Photodynamic Anticancer Agents. *Dalton Trans* 2017, 46, 11395–11407. [PubMed: 28813052]

- (33). He L; Li Y; Tan C-P; Ye R-R; Chen M-H; Cao J-J; Ji L-N; Mao Z-W Cyclometalated Iridium(III) Complexes as Lysosome-targeted Photodynamic Anticancer and Real-time Tracking Agents. *Chem. Sci* 2015, 6, 5409–5418. [PubMed: 29861886]
- (34). Nam JS; Kang MG; Kang J; Park SY; Lee SJ; Kim HT; Seo JK; Kwon OH; Lim MH; Rhee HW; Kwon TH Endoplasmic Reticulum-Localized Iridium(III) Complexes as Efficient Photodynamic Therapy Agents via Protein Modifications. *J. Am. Chem. Soc* 2016, 138, 10968–10977. [PubMed: 27494510]
- (35). Cao R; Jia J; Ma X; Zhou M; Fei H Membrane Localized Iridium(III) Complexes Induces Endoplasmic Reticulum Stress and Mitochondria-Mediated Apoptosis in Human Cancer Cells. *J. Med. Chem* 2013, 56, 3636–3644. [PubMed: 23594206]
- (36). Tian X; Zhu Y; Zhang M; Luo L; Wu J; Zhou H; Guan L; Battaglia G; Tian Y Localization Matters: A Nuclear Targeting Two-photon Absorption Iridium Complex in Photodynamic Therapy. *Chem. Commun* 2017, 53, 3303–3306.
- (37). Wilkinson AJ; Puschmann H; Howard JAK; Foster CE; Williams JAG Luminescent Complexes of Iridium(III) Containing N<sup>C</sup>N-Coordinating Terdentate Ligands. *Inorg. Chem* 2006, 45, 8685–8699. [PubMed: 17029380]
- (38). Williams JAG; Wilkinson AJ; Whittle VL Light-Emitting Iridium Complexes with Tridentate Ligands. *Dalton Trans* 2008, 2081–2099. [PubMed: 18398532]
- (39). Liu B, Monro S, Lystrom L, Cameron CG, Colon K, Yin H, Kilina S, McFarland SA, Sun W. Photophysical and Photobiological Properties of Dinuclear Iridium(III) Bis-tridentate Complexes. *Inorg. Chem* 2018, 57, 9859–9872. [PubMed: 30091916]
- (40). Collin J-P; Dixon IM; Sauvage J-P; Williams JAG; Barigelletti F; Flamigni L Synthesis and Photophysical Properties of Iridium(III) Bis(terpyridine) and Its Homologues : A Family of Complexes with a Long-Lived Excited State. *J. Am. Chem. Soc* 1999, 121, 5009–5016.
- (41). Goldstein DC; Cheng YY; Schmidt TW; Bhadbhade M; Thordarson P Photophysical Properties of a New Series of Water Soluble Iridium Bis(terpyridine) Complexes Functionalised at the 4' Position. *Dalton Trans* 2011, 40, 2053–2061. [PubMed: 21218240]
- (42). Leslie W; Batsanov AS; Howard JAK; Williams JAG Cross-couplings in the elaboration of luminescent bis-terpyridyl iridium complexes: the effect of extended or inhibited conjugation on emission. *Dalton Trans* 2004, 623–631. [PubMed: 15252526]
- (43). Lo KK-W; Chung C-K; Nga DC-M; Zhu N Syntheses, characterisation and photophysical studies of novel biological labelling reagents derived from luminescent iridium(III) terpyridine complexes. *New J. Chem* 2002, 26, 81–88.
- (44). Cavazzini M; Quici S; Scalera C; Puntoriero F; La Ganga G; Campagna S Synthesis, Characterization, Absorption Spectra, and Luminescence Properties of Multinuclear Species Made of Ru(II) and Ir(III) Chromophores. *Inorg. Chem* 2009, 48, 8578–8592. [PubMed: 19653635]
- (45). Hvasanov D; Mason AF; Goldstein DC; Bhadbhade M; Thordarson P Optimising the synthesis, polymer membrane encapsulation and photoreduction performance of Ru(II)- and Ir(III)-bis(terpyridine) cytochrome c bioconjugates. *Org. Biomol. Chem* 2013, 11, 4602–4612. [PubMed: 23715338]
- (46). Jacques A; Mesmaeker AK-D; Elias B Selective DNA Purine Base Photooxidation by Bis-terdentate Iridium(III) Polypyridyl and Cyclometalated Complexes. *Inorg. Chem* 2014, 53, 1507–1512. [PubMed: 24446771]
- (47). Matias TA; Mangoni AP; Toma SH; Rein FN; Rocha RC; Toma HE; Araki K Catalytic Water-Oxidation Activity of a Weakly Coupled Binuclear Ruthenium Polypyridyl Complex. *Eur. J. Inorg. Chem* 2016, 2016, 5547–5556.
- (48). Barbour JC; Kim AJI; DeVries E; Shaner SE; Lovaasen BM Chromium(III) Bis-Arylterpyridyl Complexes with Enhanced Visible Absorption via Incorporation of Intraligand Charge-Transfer Transitions. *Inorg. Chem* 2017, 56, 8212–8222. [PubMed: 28665604]
- (49). Peng X; Xu Y; Sun S; Wu Y; Fan J A Ratiometric Fluorescent Sensor for Phosphates: Zn<sup>2+</sup>-Enhanced ICT and Ligand Competition. *Org. Biomol. Chem* 2007, 5, 226–228. [PubMed: 17205163]

- (50). Jung HS; Han J; Shi H; Koo S; Singh H; Kim HJ; Sessler JL; Lee JY; Kim JH; Kim JS Overcoming the Limits of Hypoxia in Photodynamic Therapy: A Carbonic Anhydrase IX-Targeted Approach. *J. Am. Chem. Soc* 2017, 139, 7595–7602. [PubMed: 28459562]
- (51). Chirdon DN; Transue WJ; Kagalwala HN; Kaur A; Maurer AB; Pintauer T; Bernhard S [Ir(N<sup>^</sup>N<sup>^</sup>N)(CN)L]<sup>+</sup>: A New Family of Luminophores Combining Tunability and Enhanced Photostability. *Inorg. Chem* 2014, 53, 1487–1499. [PubMed: 24437359]
- (52). Melhuish WH Quantum Efficiencies of Fluorescence of Organic Substances: Effect of Solvent and Concentration of the Fluorescent Solute. *J. Phys. Chem* 1961, 65, 229–235.
- (53). Suzuki K; Kobayashi A; Kaneko S; Takehira K; Yoshihara T; Ishida H; Shiina Y; Oishi S; Tobita S Reevaluation of Absolute Luminescence Quantum Yields of Standard Solutions Using a Spectrometer with an Integrating Sphere and a Back-Thinned CCD Detector. *Phys. Chem. Chem. Phys* 2009, 11, 9850–9860. [PubMed: 19851565]
- (54). Carmichael I; Hug GL Triplet-Triplet Absorption Spectra of Organic Molecules in Condensed Phases. *J. Phys. Chem. Ref. Data* 1986, 15, 1–250.
- (55). Kumar CV; Qin L; Das PK Aromatic Thioketone Triplets and Their Quenching Behaviour towards Oxygen and Di-t-Butylnitroxyl Radical. A Laser-Flash-Photolysis Study. *J. Chem. Soc. Faraday Trans. 2* 1984, 80, 783–793.
- (56). Firey PA; Ford WE; Sounik JR; Kenney ME; Rodgers MAJ Silicon Naphthalocyanine Triplet State and Oxygen. A Reversible Energy-Transfer Reaction. *J. Am. Chem. Soc* 1988, 110, 7626–7630.
- (57). DeRosa MC; Crutchley RJ Photosensitized Singlet Oxygen and Its Applications. *Coord. Chem. Rev* 2002, 233–234, 351–371.
- (58). Kohn W; Sham LJ, Self-Consistent Equations Including Exchange and Correlation Effects. *Phys. Rev* 1965, 140, A1133–A1138.
- (59). Frisch MJ; Trucks GW; Schlegel HB; Scuseria GE; Robb MA; Cheeseman JR; Scalmani G; Barone V; Petersson GA; Nakatsuji H; Li X; Caricato M; Marenich AV; Bloino J; Janesko BG; GomPERT R; Mennucci B; Hratchian HP; Ortiz JV; Izmaylov AF; Sonnenberg JL; Williams-Young D; Ding F; Lipparini F; Egidi F; Goings J; Peng B; Petrone A; Henderson T; Ranasinghe D; Zakrzewski VG; Gao J; Rega N; Zheng G; Liang W; Hada M; Ehara M; Toyota K; Fukuda R; Hasegawa J; Ishida M; Nakajima T; Honda Y; Kitao O; Nakai H; Vreven T; Throssell K; Montgomery JA Jr.; Peralta JE; Ogliaro F; Bearpark MJ; Heyd JJ; Brothers EN; Kudin KN; Staroverov VN; Keith TA; Kobayashi R; Normand J; Raghavachari K; Rendell AP; Burant JC; Iyengar SS; Tomasi J; Cossi M; Millam JM; Klene M; Adamo C; Cammi R; Ochterski JW; Martin RL; Morokuma K; Farkas O; Foresman JB; Fox DJ Gaussian 16, Revision B.01, Gaussian, Inc., Wallingford CT, 2016.
- (60). Gill PMW; Johnson BG; Pople JA; Frisch MJ, The performance of the Becke-Lee-Yang-Parr (B-LYP) density functional theory with various basis sets. *Chem. Phys. Lett* 1992, 197, 499–505.
- (61). Hay PJ; Wadt WR, Ab initio effective core potentials for molecular calculations. Potentials for the transition metal atoms Sc to Hg. *J. Chem. Phys* 1985, 82, 270–283.
- (62). Clark T; Chandrasekhar J; Spitznagel GW; Schleyer PVR, Efficient diffuse function-augmented basis sets for anion calculations. III. The 3–21+G basis set for first-row elements, Li–F. *J. Comput. Chem* 1983, 4, 294–301.
- (63). Barone V; Cossi M; Tomasi J, Geometry optimization of molecular structures in solution by the polarizable continuum model. *J. Comput. Chem* 1998, 19, 404–417.
- (64). Casida ME; Jamorski C; Casida KC; Salahub DR, Molecular excitation energies to high-lying bound states from time-dependent density-functional response theory: Characterization and correction of the time-dependent local density approximation ionization threshold. *J. Chem. Phys* 1998, 108, 4439–4449.
- (65). Martin RL, Natural transition orbitals. *J. Chem. Phys* 2003, 118, 4775–4777.
- (66). Humphrey W; Dalke A; Schulten K, VMD: Visual molecular dynamics. *J. Mol. Graph* 1996, 14, 33–38. [PubMed: 8744570]
- (67). Michalec JF; Bejune SA; Cuttall DG; Summerton GC; Gertenbach JA; Field JS; Haines RJ; McMillin DR Long-Lived Emissions from 4′-Substituted Pt(Tpy)Cl<sup>+</sup> Complexes Bearing Aryl Groups. Influence of Orbital Parentage. *Inorg. Chem* 2001, 40, 2193–2200. [PubMed: 11304166]

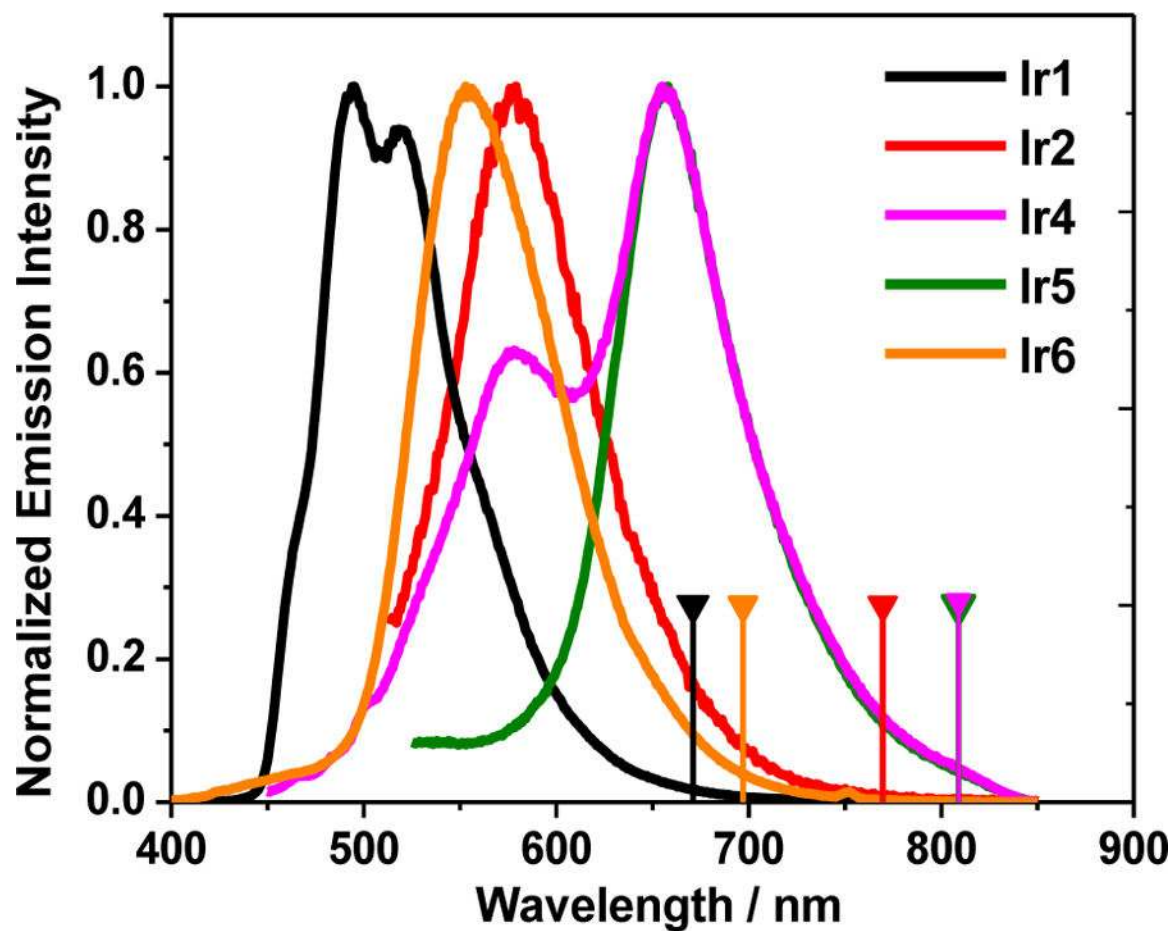
- (68). Ji Z; Li S; Li Y; Sun W Back-to-back dinuclear platinum terpyridyl complexes: Synthesis and photophysical studies. *Inorg. Chem* 2010, 49, 1337–1346. [PubMed: 20092284]
- (69). Maity D; Das S; Mardanya S; Baitalik S Synthesis, Structural Characterization, and Photophysical, Spectroelectrochemical, and Anion-Sensing Studies of Heteroleptic Ruthenium(II) Complexes Derived from 4'-Polyaromatic-Substituted Terpyridine Derivatives and 2,6-Bis(Benzimidazol-2-Yl)Pyridine. *Inorg. Chem* 2013, 52, 6820–6838. [PubMed: 23724852]
- (70). Guo F; Sun W Photophysics and Optical Limiting of Platinum(II) 4'-Arylterpyridyl Phenylacetylde Complexes. *J. Phys. Chem. B* 2006, 110, 15029–15036. [PubMed: 16869618]
- (71). Liu R; Dandu N; Li Y; Kilina S; Sun W Synthesis, Photophysics and Reverse Saturable Absorption of Bipyridyl Platinum(II) Bis(arylfluorenylacetylde) Complexes. *Dalton Trans* 2013, 42, 4398–4409. [PubMed: 23338679]
- (72). Ogilby PR; Foote CS Chemistry of Singlet Oxygen. 42. Effect of Solvent, Solvent Isotopic Substitution, and Temperature on the Lifetime of Singlet Molecular Oxygen (1Δg). *J. Am. Chem. Soc* 1983, 105, 3423–3430.
- (73). O'Brien J; Wilson I; Orton T; Pognan F Investigation of the Alamar Blue (resazurin) Fluorescent Dye for the Assessment of Mammalian Cell Cytotoxicity. *Eur. J. Biochem* 2000, 267, 5421–5426. [PubMed: 10951200]
- (74). Daghasanli NA; Itri R; Baptista MS Singlet Oxygen Reacts with 2',7'-Dichlorodihydrofluorescein and Contributes to the Formation of 2',7'-Dichlorofluorescein. *Photochem. Photobiol* 2008, 84, 1238–1243. [PubMed: 18422880]



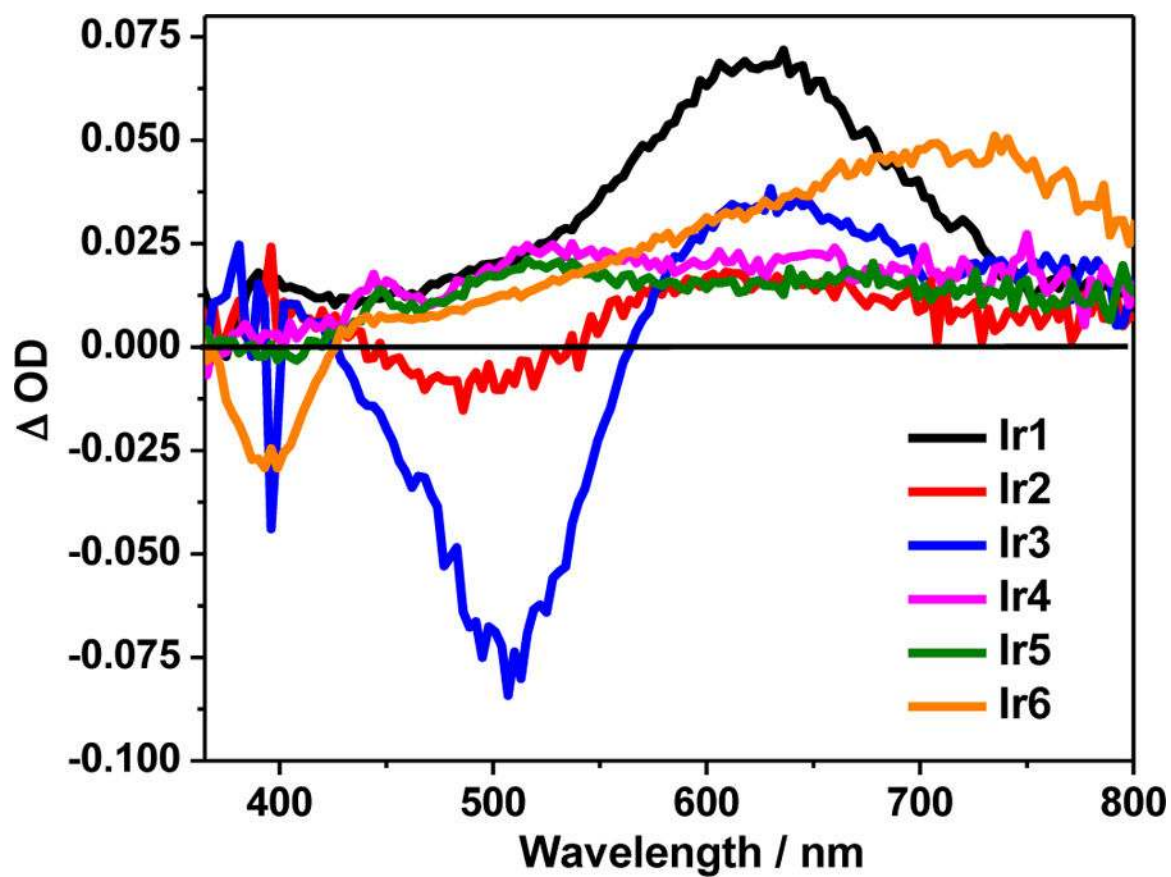
**Figure 1.**

(a) Experimental and (b) calculated absorption spectra of **Ir1–Ir6** in acetonitrile.

Calculations were carried out by linear response TDDFT using PBE1 hybrid functional with 32% HF coefficient and LAN2/DZ/6–31G\* basis sets. The simulated absorption spectra were obtained by Gaussian broadening of the calculated oscillation strength with a 0.12 eV line width.

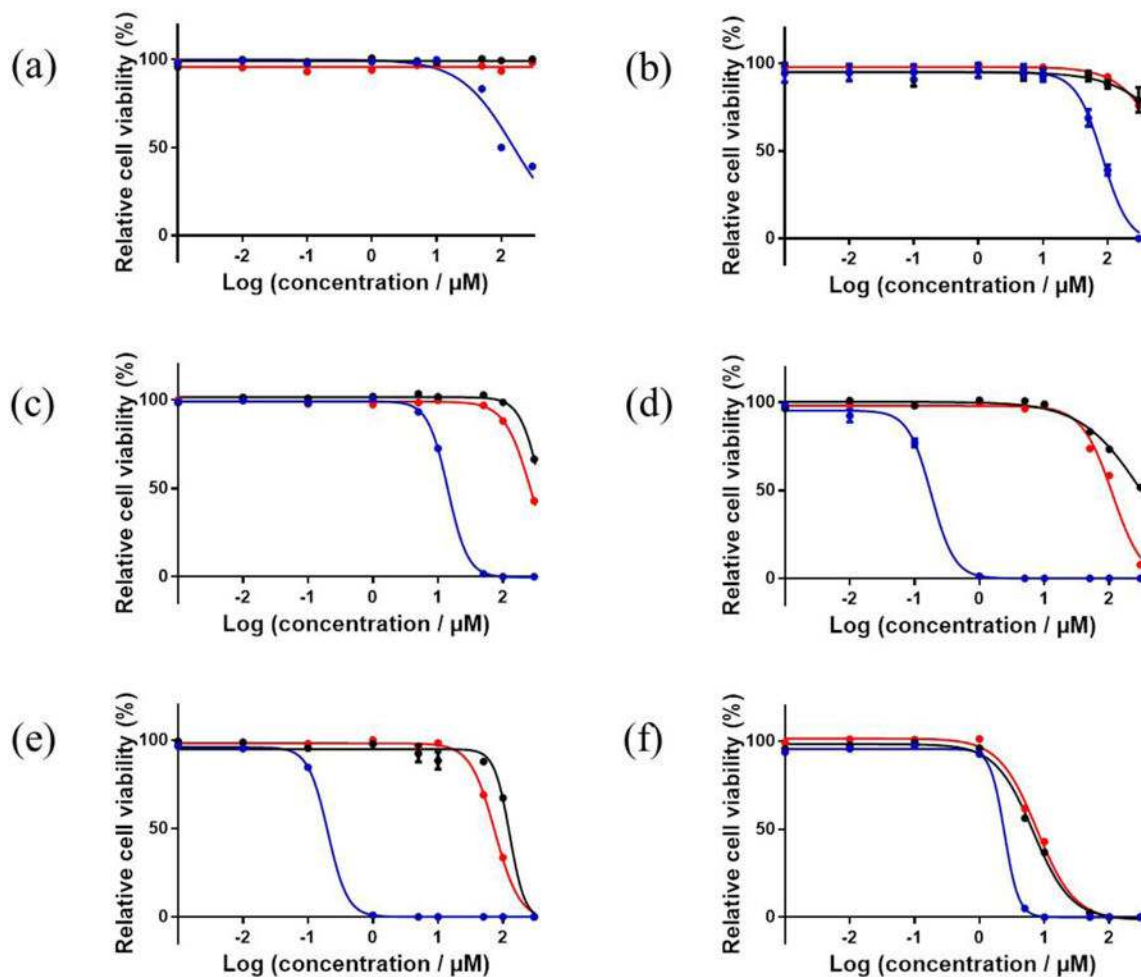


**Figure 2.** Emission spectra of **Ir1** ( $\lambda_{\text{ex}} = 369$  nm), **Ir2** ( $\lambda_{\text{ex}} = 492$  nm), **Ir4** ( $\lambda_{\text{ex}} = 434$  nm), **Ir5** ( $\lambda_{\text{ex}} = 434$  nm), and **Ir6** ( $\lambda_{\text{ex}} = 375$  nm) measured at room temperature in nitrogen purged acetonitrile ( $c = 1 \times 10^{-5}$  mol·L<sup>-1</sup>), and calculated optimized T<sub>1</sub> energy (triangle headed bar). The emission of **Ir3** was too weak to be detected. All energies were calculated by optimized excited triplet state by using PBE1 with 32% HF exchange coefficient, LAN2DZ/6-31G\* basis sets and acetonitrile solvent. Bar heights and thickness are arbitrary.

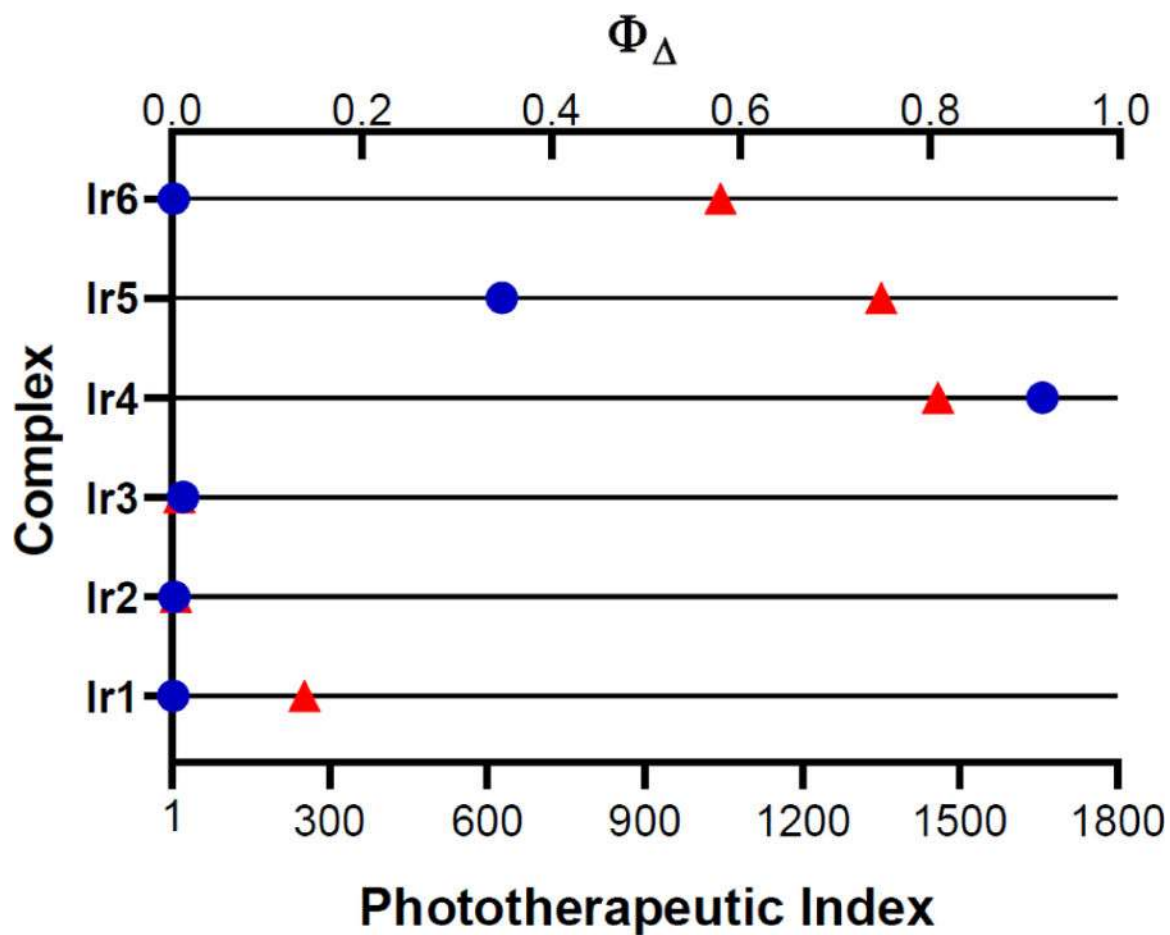


**Figure 3.** Nanosecond transient differential absorption spectra of **Ir1–Ir6** in nitrogen purged acetonitrile at zero-delay after 355 nm excitation.  $A_{355} = 0.4$  in a 1-cm cuvette.

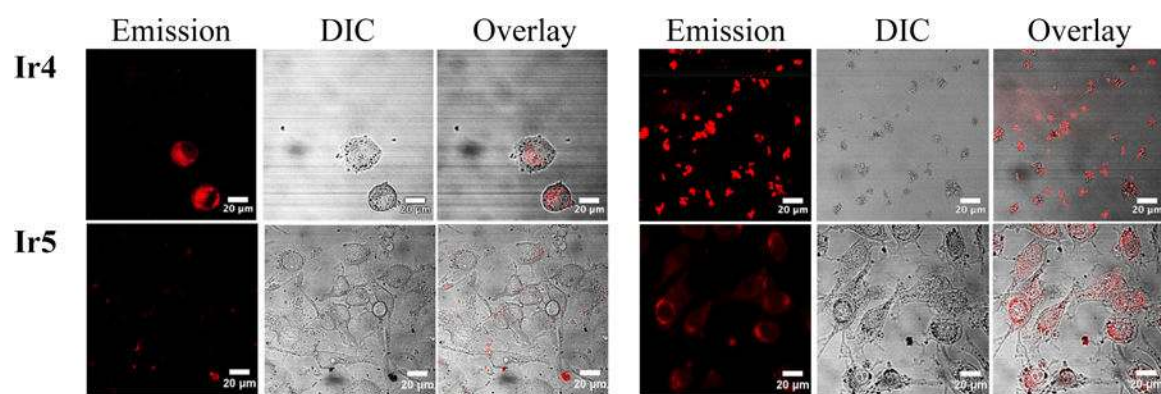




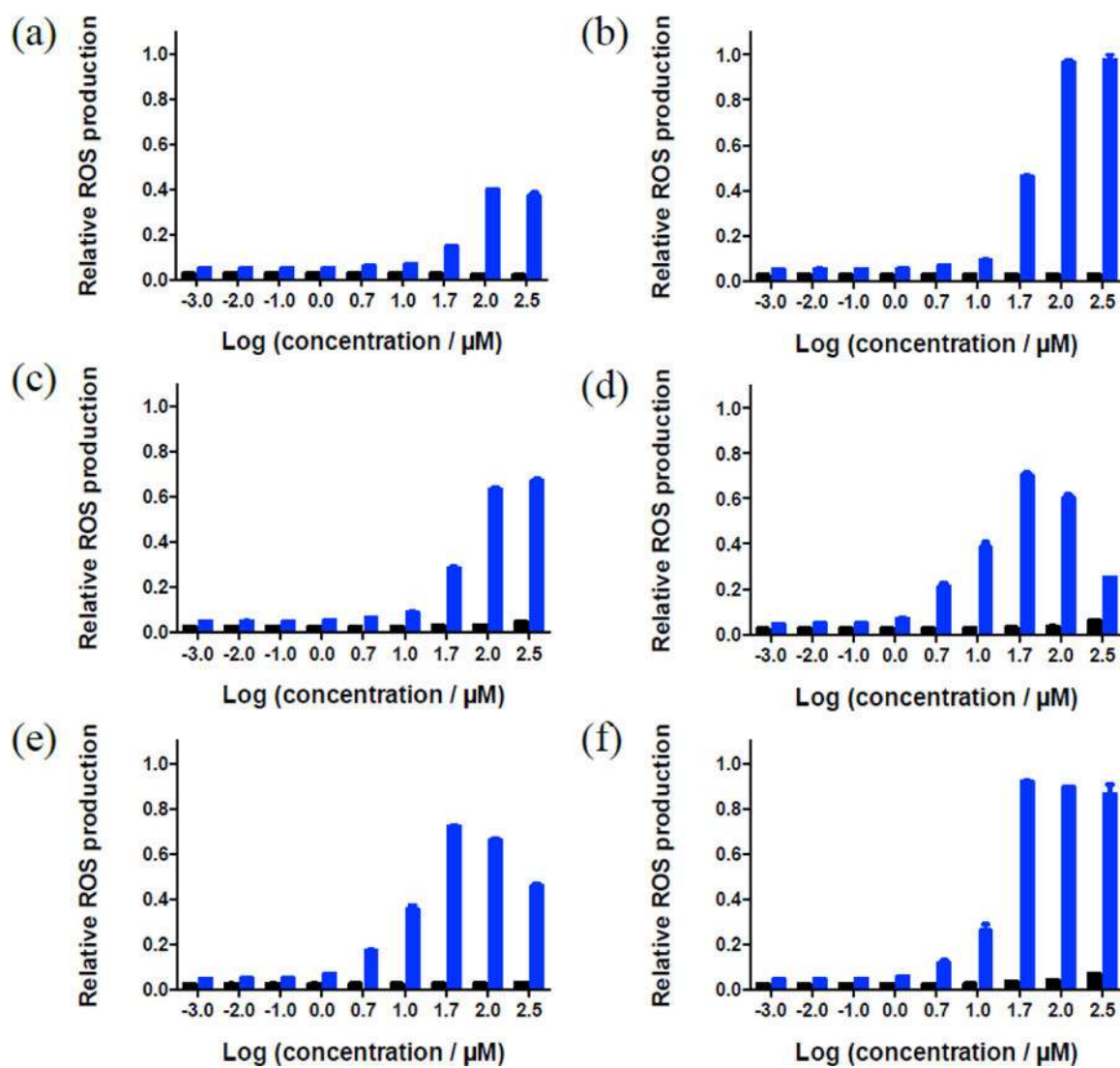
**Figure 4.** *In-vitro* dose-response curves for complexes **Ir1** (a), **Ir2** (b), **Ir3** (c), **Ir4** (d), **Ir5** (e), and **Ir6** (f) in SK-MEL-28 cells without (black) or with visible (blue) or red (red) light irradiation.



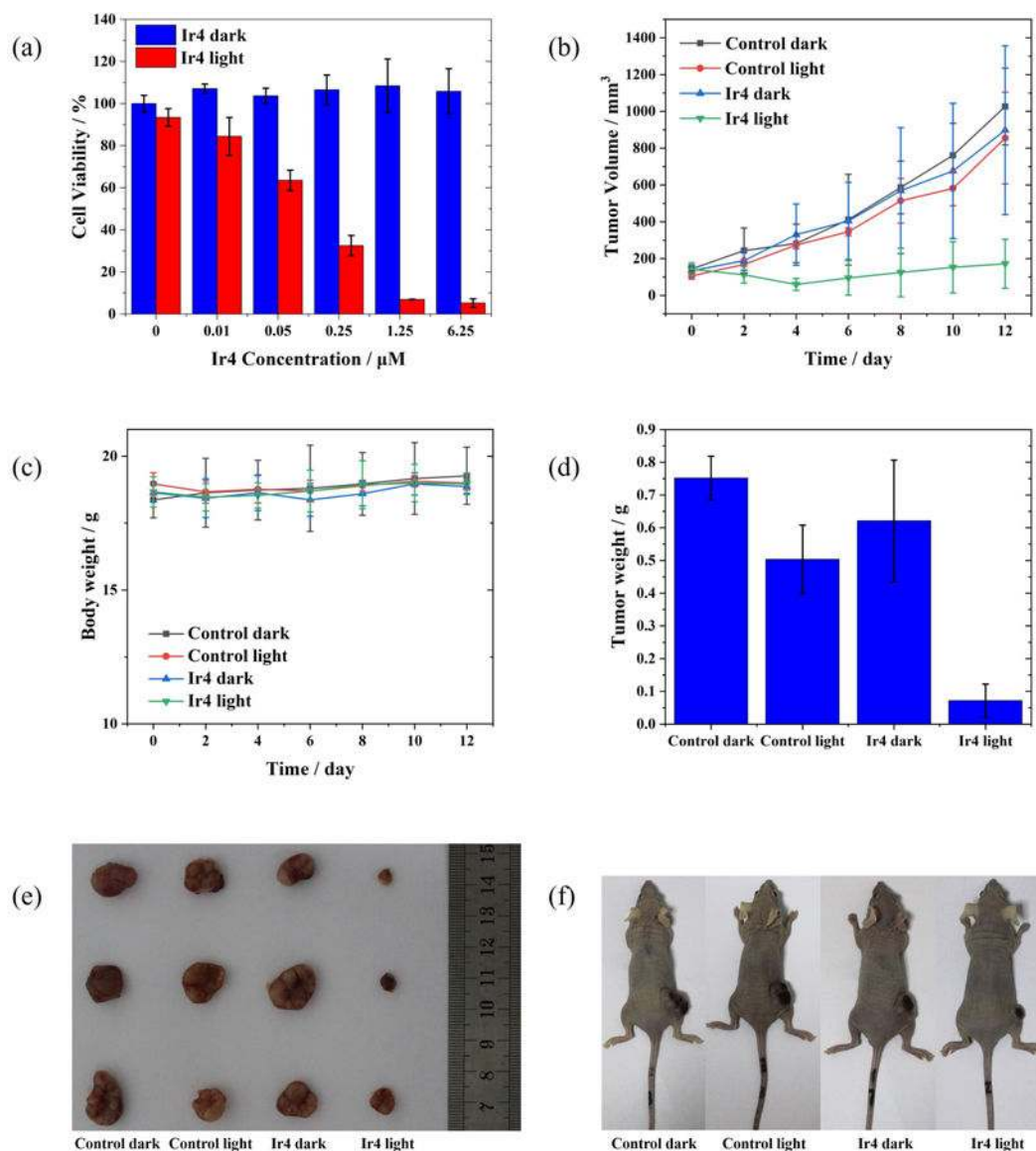
**Figure 5.** Correlation chart between the cell-free  $^1\text{O}_2$  quantum yields (red triangles) and the *in vitro* PIs (blue circles) for complexes **Ir1-Ir6**.



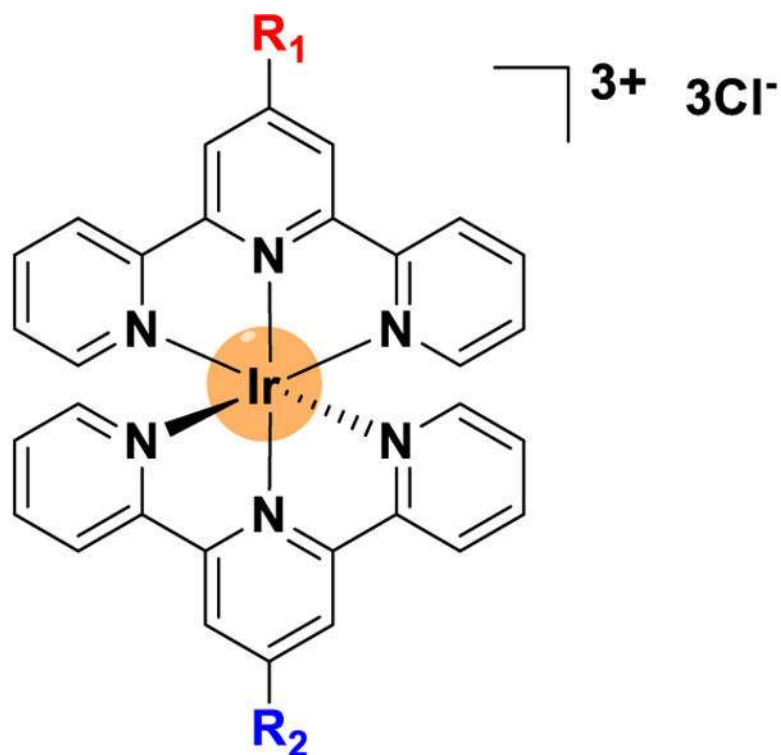
**Figure 6:**  
Confocal luminescence images of SK-MEL-28 cells dosed with complexes **Ir4** and **Ir5** (50  $\mu\text{M}$ ) in the dark (left) and with visible light (50  $\text{J cm}^{-2}$ ) (right).



**Figure 7.** ROS assay results (60 min post-treatment) for SK-MEL-28 cells treated with **Ir1** (a), **Ir2** (b), **Ir3** (c), **Ir4** (d), **Ir5** (e), and **Ir6** (f). DCFDA was used as a ROS probe. The black bars and blue bars represent the results for cells treated in the dark or with 50 J cm<sup>-1</sup> visible light, respectively.

**Figure 8.**

(a) Dose-dependent cell viability study of **Ir4** toward MCF-7 breast cancer cells. The light treatment used a 450-nm 50- $\text{mW cm}^{-2}$  blue light to irradiate for 5 mins. ( $15 \text{ J cm}^{-2}$ ). (b) Tumor growth curves of the four differently treated mouse groups. (c) Body weight changes of the four differently treated mouse groups. (d) Comparison of the tumor weight 12 days after different treatments. (e) Photographs of tumors collected from the mice 12 days after the different treatments. (f) Photographs of tumor-bearing mice 12 days after the different treatments. In panels b-f, all of the light treatments used a 450-nm 100  $\text{mW cm}^{-2}$  blue light to irradiate for 10 mins ( $60 \text{ J cm}^{-2}$ ).



**Ir1:  $R_1 = R_2 = \text{Ph}$**

**Ir2:  $R_1 = 4\text{'-N(CH}_3)_2\text{Ph}$ ,  $R_2 = \text{Ph}$**

**Ir3:  $R_1 = R_2 = 4\text{'-N(CH}_3)_2\text{Ph}$**

**Ir4:  $R_1 = \text{Pyren-1-yl}$ ,  $R_2 = \text{Ph}$**

**Ir5:  $R_1 = R_2 = \text{Pyren-1-yl}$**

**Ir6:  $R_1 = 4\text{'-CH}_3(\text{OCH}_2\text{CH}_2)_3\text{OPh}$ ,  $R_2 = \text{Ph}$**

**Chart 1.**

Structures of Homo- and Heteroleptic Ir(III) Bis(terpyridine) Complexes Ir1–Ir6.

**Table 1.**Electronic Absorption, Emission, and Triplet Excited-State Absorption Parameters for Complexes **Ir1–Ir6**.

	$\lambda_{\text{abs}}/\text{nm}$ (log $\epsilon$ ) <sup>a</sup>	$\lambda_{\text{em}}/\text{nm}$ ( $\tau_{\text{em}}/\mu\text{s}$ ); $\Phi_{\text{em}}$ <sup>b</sup>	$\lambda_{\text{T1-Tn}}/\text{nm}$ ( $\tau_{\text{TA}}/\mu\text{s}$ ) <sup>c</sup>	$\Phi_{\Delta}$ ( $\lambda_{\text{ex}}/\text{nm}$ ) <sup>d</sup>
<b>Ir1</b>	296 (4.77); 318 (4.67); 338 (4.58); 369 (4.32)	494 (2.54), 519 (-); 0.32 <sup>e</sup>	389 (-), 636 (2.25)	0.14 (340)
<b>Ir2</b>	298 (4.76); 318 (4.73); 364 (4.11); 493 (4.42)	578 (3.13); < 0.001	611 (0.009), 627 (3.12)	0.004 (475)
<b>Ir3</b>	283 (4.73); 310 (4.76); 320 (4.78); 503 (4.70)	– <sup>f</sup>	630 (0.008)	0.008 (478)
<b>Ir4</b>	280 (4.92); 323 (4.79); 338 (4.79); 440 (4.11)	577 (– <sup>g</sup> ); 655 (– <sup>f</sup> ); 0.008	444 (-), 528 (5.79)	0.81 (450)
<b>Ir5</b>	280 (5.06); 325 (4.94); 338 (4.95); 434 (4.40)	655 (– <sup>f</sup> ); 0.004	444 (-), 527 (24.5)	0.75 (450)
<b>Ir6</b>	280 (4.77); 295 (4.71); 318 (4.64); 375 (4.42)	557 (7.92); 0.078	735 (8.15)	0.58 (386)

<sup>a</sup> $\lambda_{\text{abs}}$  refers to the electronic absorption band maxima and  $\epsilon$  indicates the molar extinction coefficients. The measurements were carried out in CH<sub>3</sub>CN at room temperature.

<sup>b</sup> $\lambda_{\text{em}}$  and  $\tau_{\text{em}}$  are the emission band maxima and lifetimes, respectively, at room temperature in degassed CH<sub>3</sub>CN solutions ( $c = 1 \times 10^{-5}$  mol·L<sup>-1</sup>). For determining the emission quantum yields, the reference used was a degassed acetonitrile solution of [Ru(bpy)<sub>3</sub>]Cl<sub>2</sub> ( $\Phi_{\text{em}} = 0.097$ ,  $\lambda_{\text{ex}} = 436$  nm).

<sup>c</sup>Nanosecond TA band maxima ( $\lambda_{\text{T1} \rightarrow \text{Tn}}$ ) and triplet excited state lifetimes ( $\tau_{\text{TA}}$ ) measured in degassed CH<sub>3</sub>CN at room temperature.

<sup>d</sup>Singlet oxygen quantum yields in acetonitrile, with [Ru(bpy)<sub>3</sub>](PF<sub>6</sub>)<sub>2</sub> in aerated CH<sub>3</sub>CN ( $\Phi_{\Delta} = 0.56$ ) being used as the standard sample. The results are corrected to within  $\pm 5\%$ .

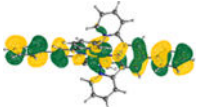

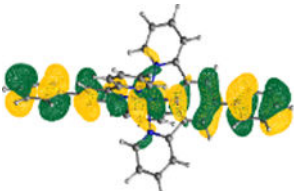

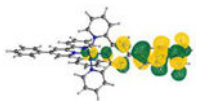

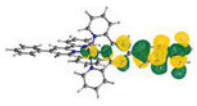
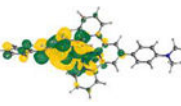
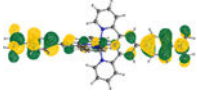
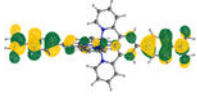
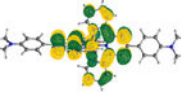
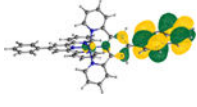
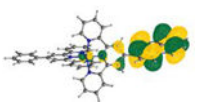
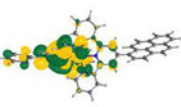
<sup>e</sup>Quinine bisulfate ( $\lambda_{\text{ex}} = 347.5$  nm,  $\Phi_{\text{em}} = 0.546$ ) in 1N H<sub>2</sub>SO<sub>4</sub> solution was used as the reference.

<sup>f</sup>Emission signals were too weak to be measured upon 355-nm excitation on our laser flash photolysis spectrometer, which is not optimized for emission measurements.

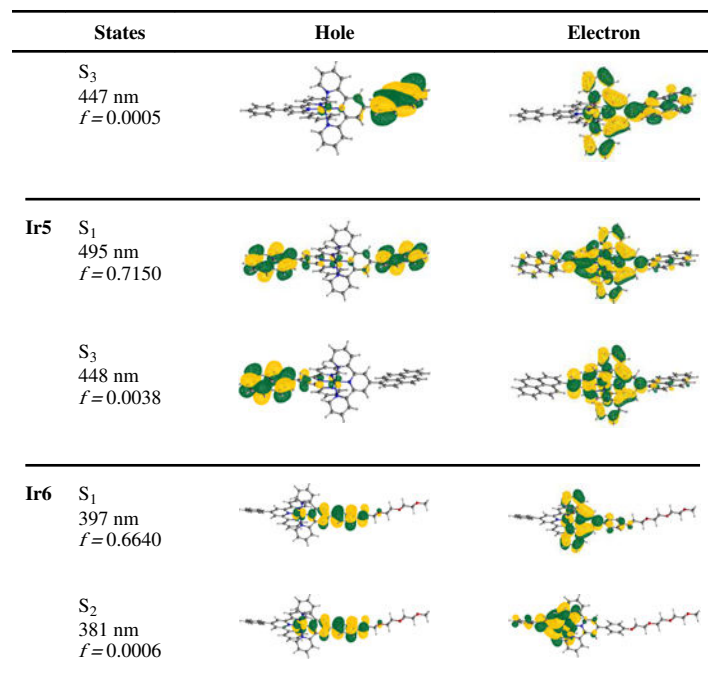
<sup>g</sup>Lifetime was too short to be measured on our instrument.

**Table 2.**

Natural Transition Orbitals (NTOs) for the Major Transitions Contributing to the Low-Energy Absorption Band of Complexes Ir1–Ir6 in CH<sub>3</sub>CN.



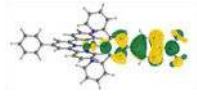
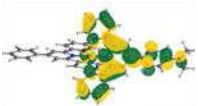
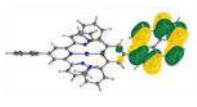
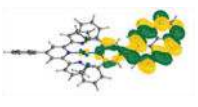
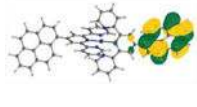
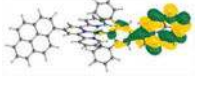


	States	Hole	Electron
<b>Ir1</b>	S <sub>1</sub> 338 nm <i>f</i> = 0.8886		
		55%	55%
	S <sub>2</sub> 337 nm <i>f</i> = 0.0060		
		44%	44%
<b>Ir2</b>	S <sub>1</sub> 500 nm <i>f</i> = 0.6113		
			
	S <sub>2</sub> 497 nm <i>f</i> = 0.0508		
	<b>Ir3</b>	S <sub>1</sub> 505 nm <i>f</i> = 1.2774	
			
S <sub>3</sub> 479 nm <i>f</i> = 0.0001			
<b>Ir4</b>		S <sub>1</sub> 490 nm <i>f</i> = 0.3467	
			
	S <sub>2</sub> 448 nm <i>f</i> = 0.0028		





**Table 3.**

NTOs of the Lowest Triplet Excited State ( $T_1$ ) of Ir1-Ir6 in  $\text{CH}_3\text{CN}$ . Modified PBE1 Functional with 32% HF Exchange Coefficient and LAN2DZ/6-31G\* Basis Sets Were Used for the Calculations.

	$T_1$ / nm	Hole	Electron
Ir1	671		
Ir2	769		
Ir4	780		
Ir5	782		
Ir6	697		

**Table 4.**

EC<sub>50</sub> values ( $\mu\text{M}$ ) for SK-MEL-28 cancer cells dosed with complexes **Ir1–Ir6**.

	Dark	Vis <sup>a</sup>	PI <sup>b</sup>	Red <sup>c</sup>	PI <sup>d</sup>
<b>Ir1</b>	> 300	153 ± 15	> 2	> 300	1
<b>Ir2</b>	> 300	83.4 ± 4.2	> 4	> 300	1
<b>Ir3</b>	> 300	14.2 ± 0.2	> 21	266	> 1
<b>Ir4</b>	> 300	0.18 ± 0.01	> 1657	112 ± 4	> 3
<b>Ir5</b>	127 ± 5	0.20 ± 0.01	628	75.1 ± 1.1	2
<b>Ir6</b>	6.72 ± 0.22	2.42 ± 0.08	3	7.65 ± 0.29	1

<sup>a</sup>Vis-PDT: 16 hours drug-to-light interval followed by 100 J·cm<sup>-2</sup> broadband visible light irradiation,

<sup>b</sup>PI = phototherapeutic index (ratio of dark EC<sub>50</sub> to visible-light EC<sub>50</sub>),

<sup>c</sup>Red-PDT: 16 hours drug-to-light interval followed by 100 J·cm<sup>-2</sup> light irradiation with 625-nm LEDs,

<sup>d</sup>PI = phototherapeutic index (ratio of dark EC<sub>50</sub> to red-light EC<sub>50</sub>)